

## HOST GALAXIES OF THE HIGH-REDSHIFT AGNS IN THE GOODS FIELDS

MASAYUKI AKIYAMA<sup>1</sup>

Subaru Telescope, National Astronomical Observatory of Japan, Hilo, HI, 96720

Accepted for publication in *ApJ*

### ABSTRACT

The star-formation rates and the stellar masses of the host galaxies of active galactic nuclei (AGNs) at high-redshifts are keys to understanding the evolution of the relation between the mass of the spheroidal component of a galaxy and the mass of its central black hole ( $M_{\text{bulge}} - M_{\bullet}$  relation). We investigate the host galaxies of 31 AGNs with spectroscopic redshifts between 2 and 4 found in the deep *Chandra* surveys of the Great Observatories Origins Deep Surveys (GOODS) fields. We use the F606W, F775W, and F850LP band images obtained with the Advanced Camera for Surveys (ACS) on the Hubble Space Telescope (HST). The sample can be divided into 17 “extended” AGNs and 14 “compact” AGNs based on the concentration parameter defined as the difference between the aperture magnitudes with 0.''07 and 0.''25 diameter. We derive upper limits of the UV luminosities of the host galaxies of the “compact” AGN sample, and upper and lower limits of the UV luminosities of the host galaxies of the “extended” AGN sample. These limits are consistent with the knee of the luminosity function of the Lyman Break Galaxies (LBGs) at  $z \sim 3$ , suggesting moderate star-formation rates, less than  $40 M_{\odot} \text{ yr}^{-1}$ , in the host galaxies of the AGNs at  $2 < z_{\text{sp}} < 4$  without correcting the dust extinction. By combining the limits of the UV luminosities with the observed *K*-band magnitudes for the “extended” AGNs, we derive the upper and lower limits of the stellar masses of their host galaxies. The derived upper limits on the stellar masses range from  $10^{10} M_{\odot}$  to  $10^{12} M_{\odot}$ . The upper limits imply that the  $M_{\text{bulge}} - M_{\bullet}$  relation of the high-redshift AGNs is different from that of the galaxies in the nearby universe or the average Eddington ratio of the high-redshift AGNs is higher than that of low-redshift AGNs with lower-luminosity.

*Subject headings:* galaxies:active — galaxies:photometry — galaxies:high-redshift — quasars:general

### 1. INTRODUCTION

Formation processes of massive black holes at the centers of galaxies have been one of important issues in astronomy, especially after the discovery of massive black holes in the centers of many massive galaxies (Kormendy & Richstone 1995). The formation processes are thought to link with the formation of the bulges of the host galaxies. The correlations between an absolute magnitude of a spheroidal component of a galaxy and the mass of the central black hole (Magorrian et al. 1998; Marconi & Hunt 2003; Haring & Rix 2004) and between the stellar velocity dispersion of the spheroidal component and the black hole mass (Gebhardt et al. 2000; Merritt & Ferrarese 2001) suggest that the ratio between the stellar mass of the spheroidal component of a galaxy and the mass of its central black hole is constant (e.g.  $M_{\bullet}/M_{\text{bulge}} = 0.0014$ ; Haring & Rix 2004; hereafter  $M_{\text{bulge}} - M_{\bullet}$  relation). Moreover, the similarity between the cosmic evolutions of the star formation rate density and of the number density of luminous quasi stellar objects (QSOs) suggests that the co-evolution of the stellar component and the central black hole in a galaxy (e.g., Boyle & Terlevich 1998; Franceschini et al. 1999).

Active Galactic Nuclei (AGNs) are important sites of black hole growth. The mass density of the central black holes of galaxies in the nearby universe can be explained with the mass accretion in the observed AGNs integrated over cosmic time (Yu & Tremaine 2002; Barger et al. 2001; Marconi et al. 2004). Thus by studying the relation between the accretion parameters of AGNs and properties of their host galaxies, we can directly reveal whether the central black holes and the spheroidal components of galaxies really grow synchronously.

For example, by comparing the star formation rate of each host galaxy with the nuclear accretion rate, we can statistically connect the growth of stellar masses in galaxies and that of the masses of their central black holes. Discoveries of strong far-infrared (FIR) continuum emission (e.g., Isaak et al. 2002; Omont et al. 2002; Bertoldi et al. 2003) of high-redshift ( $1.8 < z < 6.4$ ) ultra-luminous (*B*-band absolute magnitudes,  $M_B < -26$ ) QSOs indicate that violent star-formation (star formation rate up to  $3000 M_{\odot} \text{ yr}^{-1}$ ) is associated with the QSO activity. This means that black holes in a rapid growth phase reside in host galaxies under violent star-formation phase. By contrast, for QSOs with modest luminosity ( $-25.3 < M_B < -21.5$ ), the Hubble Space Telescope (HST) optical imaging observations of QSOs at  $z \sim 2$  found in the Galaxy Evolution from Morphologies and SEDs (GEMS) survey field reveal modest star formation in their host galaxies (Jahnke et al. 2004). They reside in host galaxies with object-frame UV wavelength luminosity similar to those of Lyman Break Galaxies (LBGs) at  $z \sim 3$ . The corresponding star-formation rate is  $2 \sim 16 M_{\odot} \text{ yr}^{-1}$  without correcting the dust extinction with an assumption that the UV emission comes from young stars under continuous star formation (Jahnke et al. 2004). Star-formation activity in a QSO host galaxy may correlate with the luminosity of the QSO (e.g., Yamada 1994).

For AGNs, the  $M_{\text{bulge}} - M_{\bullet}$  relation at high-redshifts can be directly examined. If the central black hole and the spheroidal component of a galaxy really grow synchronously, the  $M_{\text{bulge}} - M_{\bullet}$  relation does not change with redshifts. If not, it is possible that either of the central black hole or the spheroidal component grow faster than the other in the early stage of their formation. In this case the  $M_{\text{bulge}} - M_{\bullet}$  relation at high-redshifts can be different from that in the nearby universe. Current observing facilities can not resolve the central stellar motion of high-redshift galaxies as high spatial resolu-

Electronic address: akiyama@subaru.naoj.org

<sup>1</sup> Also, Institute for Astronomy, University of Hawaii

tion as for galaxies in the nearby universe, thus we are not able to directly measure  $M_{\bullet}$  of the high-redshift galaxies. However, for galaxies with an AGN, the velocity width of the AGN broad emission line and/or luminosity of the AGN can provide us precious information on the mass of the central black hole in a high-redshift galaxy.

The near-infrared (NIR) imaging observations of QSOs at  $z = 1 \sim 2$  have been done with the NICMOS (Near Infrared Camera and Multi Object Spectrometer) on the HST (Kukula et al. 2001; Ridgway et al. 2001) and with ground-based 8-10m class telescopes with adaptive optics (AO) systems (Croom et al. 2004) or under good natural seeing condition (Falomo et al. 2004). Kukula et al. (2001) observe radio-loud and radio-quiet QSOs with  $M_B = -23.8 \text{--} -24.8$  mag at  $z < 0.5$ ,  $z = 1$ , and  $z = 2$ , and find that the object-frame  $V$ -band absolute magnitudes of the radio-loud QSOs at  $z \sim 1$  and  $z \sim 2$  are more luminous than low-redshift ( $z < 0.5$ ) counterpart on average and are consistent with the passive evolution model of a galaxy with  $4L_V^*$  formed at  $z_f = 5$ . On the other hand, the average absolute magnitudes of host galaxies of radio-quiet QSOs do not change significantly up to redshift 2, and 1 magnitude fainter than the  $z_f = 5$  passive evolution model scaled to the absolute magnitudes of QSO host galaxies in the nearby universe ( $3L_V^*$  at  $z < 0.5$ ). Similar results are suggested by Ridgway et al. (2001) for QSOs with  $M_B = -22 \text{--} -24$  mag. The upper limits of the brightnesses of host galaxies obtained by Croom et al. (2004) for QSOs with  $M_B = -24.5 \text{--} -27$  are consistent with the faint radio-quiet QSO host galaxies. Falomo et al. (2004) observed QSOs with  $M_B = -25.5 \text{--} -28$  at  $z \sim 2$  and do not find significant evolutionary difference between radio-loud and radio-quiet QSOs, although host galaxy absolute magnitudes of radio-quiet QSOs are not significantly different from those by Kukula et al. (2001). The faint host galaxies of high-redshift radio-quiet QSOs imply that the stellar masses of the host galaxies are smaller than those of the nearby galaxies with the same black hole mass. It is also possible that the  $M_{\text{bulge}} - M_{\bullet}$  relation does not change at high-redshifts, and the Eddington ratio, ratio between the bolometric luminosity and the Eddington luminosity ( $\lambda \equiv L_{\text{bol}}/L_E$ ), is higher for high-redshift AGNs ( $\lambda = 1$ ) than for low-redshift counterparts ( $\lambda = 0.1 \sim 0.01$ ; e.g. Schade et al. 2000). The  $M_{\text{bulge}} - M_{\bullet}$  relation at  $z > 2$  is examined with bulge velocity dispersion inferred from velocity width of the narrow [OIII] $\lambda 5007$  emission line and the black hole mass inferred from broad  $H\beta$  emission line and optical luminosity (Shields et al. 2003). The result suggests no significant change in the relationship between black hole mass and bulge velocity dispersion up to redshift 3, although the dispersion of the distribution is large ( $\pm 1$  dex; Shields et al. 2003). These studies on the star formation rates and the stellar masses of the host galaxies of QSOs at high-redshift are limited in number and limited to optically-selected classical QSOs so far.

In this paper, we examine star-formation rates and stellar masses of the host galaxies of X-ray-selected high-redshift AGNs in the GOODS, the Great Observatories Origins Deep Survey, fields, in order to expand the sample number of host galaxies of high- $z$  AGNs, and to extend the study to AGN selected in the X-ray band. Thanks to ultra-deep X-ray surveys with *Chandra* (Alexander et al. 2003; Giacconi et al. 2002) and intensive spectroscopic follow-up observations with 8-10m class telescopes (Barger et al. 2003; Szokoly et al. 2003), 31 AGNs are found in the redshift range  $2 < z_{\text{sp}} < 4$  in the fields. The luminosities of the AGNs range from as faint as Seyfert galaxies (luminosity in the hard X-

ray band,  $L_{2-10\text{keV}} < 10^{44}$  erg  $\text{s}^{-1}$ ) to as luminous as QSOs ( $L_{2-10\text{keV}} > 10^{44}$  erg  $\text{s}^{-1}$ ), covering the most important population of AGNs whose contribution to the Cosmic X-ray Background is significant (Ueda et al. 2003), i.e. they represent important part of the cosmic accretion history. Moreover, the deep high-resolution imaging observations with the Advanced Camera for Surveys (ACS) on the HST in the fields (Giavalisco et al. 2004) enable us to examine the properties of the host galaxies of the high- $z$  AGNs.

Since X-ray-selection of AGNs is less affected by the absorption to their nucleus than optical-selection, the X-ray selected samples includes obscured narrow-line AGNs as well as non-obscured broad-line AGNs. For luminous non-obscured AGNs, due to the bright nuclear stellar component of the optical image, it is quite difficult to directly examine the properties of the host galaxies, especially for high- $z$  AGNs. Even with the HST, still the size of the point spread function (PSF) (FWHM is  $0.''10$ ) is comparable to a 1kpc scale ( $0.''12$  at  $z = 2$  and  $0.''14$  at  $z = 4$ ). Additionally, the physical sizes of high-redshift galaxies are smaller than those of nearby galaxies on average. Thus, we evaluate only the upper limits of the brightnesses of the host galaxies in Section 3.2.

On the other hand, obscured AGNs show relatively faint nuclear stellar component with extended host galaxy component, thus we can examine the nature of the host galaxies more directly than for non-obscured AGNs. However, it is difficult to evaluate the contribution from the nuclear point source to the total image in this case. Therefore, we evaluate the lower and upper limits on the brightnesses of the host galaxies in Section 3.3.

We derive the constraints on the star-formation rates of the host galaxies from the upper and lower limits of the object-frame UV brightnesses. Moreover, using the F606W, F775W, F850LP, and  $K$ -bands photometry, we derive limits on the stellar masses of the host galaxies and discuss the relation between stellar masses of the host galaxies and black hole masses of the AGNs. Throughout the paper, we use the cosmological parameters,  $\Omega_m = 0.3$ ,  $\Omega_{\Lambda} = 0.7$ , and  $H_0 = 70$  km  $\text{s}^{-1}$  Mpc $^{-1}$ . All magnitudes are on the AB magnitude system.

## 2. SAMPLES AND DATA

High-redshift AGNs are selected from the catalogs of spectroscopically-identified optical counterparts of X-ray sources found in the ultra-deep *Chandra* surveys in the GOODS North (GOODSN; Barger et al. 2003) and GOODS South (GOODSS; Szokoly et al. 2003) fields. The flux limits of the surveys reach  $2.5 \times 10^{-17}$  erg  $\text{s}^{-1}$   $\text{cm}^{-2}$  (0.5–2 keV) and  $1.4 \times 10^{-16}$  erg  $\text{s}^{-1}$   $\text{cm}^{-2}$  (2–10 keV) in the on-axis area of GOODSN field with 2Ms exposure time, and  $5.2 \times 10^{-17}$  erg  $\text{s}^{-1}$   $\text{cm}^{-2}$  (0.5–2 keV) and  $2.8 \times 10^{-16}$  erg  $\text{s}^{-1}$   $\text{cm}^{-2}$  (2–10 keV) in the on-axis area of GOODSS field with 1Ms exposure time (Alexander et al. 2003).

In the GOODSN and GOODSS regions, optical images obtained with the ACS through the F435W, F606W, F775W, and F850LP-band filters are available. Based on the transmission curves of the filters and the response function of the CCD detector of the ACS, we estimate the effective wavelengths of the F435W, F606W, F775W, and F850LP-band images are 4301Å, 5926Å, 7705Å, and 9037Å, respectively, for an object with a flat optical spectrum.

In order to escape from the incompleteness of the optical identification in the redshift range between  $1.4 < z < 2.0$ , i.e. “redshift desert”, we set the lower redshift limit of our sample as 2. The upper redshift limit is determined to be 4, because

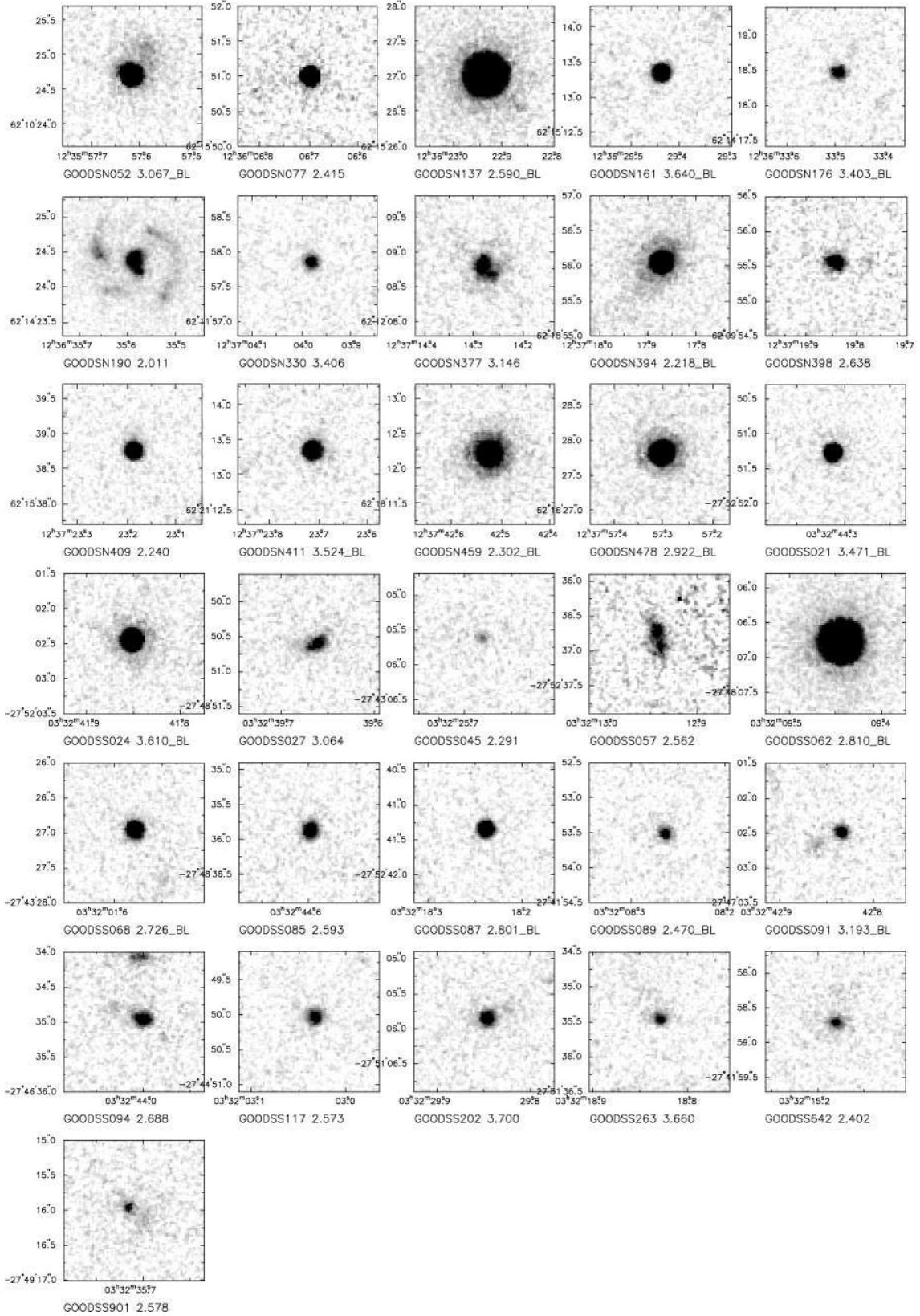


FIG. 1.— F775W band images of the AGNs at  $2 < z_{sp} < 4$  in the GOODS fields. Field of view is  $4'' \times 4''$  with north is up and east is left. The name and the redshift are shown in the bottom of each panel. AGNs with a broad-emission line in the optical spectrum are indicated with “BL”.

TABLE 1  
HIGH REDSHIFT AGN SAMPLE IN THE GOODS FIELDS

Name	GOODS Ver.1.0 Cat. ID.	$z$	$F_{0.5-8\text{keV}}^a$	$L_{2-10\text{keV}}^b$	$K_{AB}^c$	Note <sup>d</sup>
GOODSN052	J123557.62+621024.7	3.067	$1.10^{+0.13}_{-0.14}$	$43.90^{+0.05}_{-0.05}$	22.33	BLAGN
GOODSN077	J123606.70+621551.0	2.415	$1.69^{+0.10}_{-0.11}$	$43.82^{+0.03}_{-0.03}$	21.73	
GOODSN137	J123622.94+621527.0	2.590	$18.80^{+0.32}_{-0.32}$	$44.95^{+0.01}_{-0.01}$	20.33	BLAGN
GOODSN161	J123629.44+621513.3	3.640	$1.99^{+0.11}_{-0.11}$	$44.35^{+0.02}_{-0.02}$	22.63	BLAGN
GOODSN176	J123633.50+621418.4	3.403	$1.16^{+0.09}_{-0.09}$	$44.04^{+0.04}_{-0.03}$	23.73	BLAGN
GOODSN190	J123635.59+621424.3	2.011 <sup>e</sup>	$2.52^{+0.18}_{-0.19}$	$43.79^{+0.03}_{-0.03}$	21.03	
GOODSN330	J123703.99+621157.8	3.406	$0.32^{+0.08}_{-0.09}$	$43.48^{+0.12}_{-0.11}$	23.13	
GOODSN377	J123714.28+621208.8	3.146	$0.79^{+0.08}_{-0.08}$	$43.79^{+0.05}_{-0.05}$	21.93	
GOODSN394	J123717.88+621856.0	2.218	$9.95^{+0.26}_{-0.27}$	$44.50^{+0.01}_{-0.01}$	21.43	BLAGN
GOODSN398	J123719.84+620955.5	2.638	$3.38^{+0.18}_{-0.19}$	$44.22^{+0.02}_{-0.02}$	22.23	
GOODSN409	J123723.19+621538.7	2.240	$1.77^{+0.13}_{-0.14}$	$43.76^{+0.03}_{-0.03}$	22.13	
GOODSN411	J123723.72+622113.3	3.524	$1.60^{+0.17}_{-0.18}$	$44.22^{+0.05}_{-0.05}$	22.83	BLAGN
GOODSN459	J123742.53+621812.2	2.302	$20.80^{+0.39}_{-0.40}$	$44.86^{+0.01}_{-0.01}$	20.93	BLAGN
GOODSN478	J123757.31+621627.8	2.922	$4.68^{+0.19}_{-0.19}$	$44.48^{+0.02}_{-0.02}$	20.73	BLAGN
GOODSS021	J033244.31-275251.3	3.471	$1.21^{+0.14}_{-0.15}$	$44.08^{+0.05}_{-0.05}$	23.30 <sup>f</sup>	BLAGN
GOODSS024	J033241.85-275202.5	3.610	$5.73^{+0.35}_{-0.35}$	$44.80^{+0.03}_{-0.03}$	21.31 <sup>f</sup>	BLAGN
GOODSS027	J033239.67-274850.6	3.064	$7.56^{+0.45}_{-0.47}$	$44.74^{+0.03}_{-0.03}$	21.61 <sup>f</sup>	
GOODSS045	J033225.68-274305.7	2.291	$6.12^{+0.38}_{-0.40}$	$44.32^{+0.03}_{-0.03}$	21.73 <sup>f</sup>	
GOODSS057	J033212.94-275236.9	2.562	$5.53^{+0.37}_{-0.40}$	$44.41^{+0.03}_{-0.03}$	22.64	
GOODSS062	J033209.45-274806.8	2.810	$7.11^{+0.39}_{-0.41}$	$44.62^{+0.02}_{-0.02}$	19.64	BLAGN
GOODSS068	J033201.58-274327.0	2.726	$8.59^{+0.38}_{-0.40}$	$44.67^{+0.02}_{-0.02}$	22.55	BLAGN
GOODSS085	J033244.60-274835.9	2.593	$1.86^{+0.18}_{-0.20}$	$43.95^{+0.04}_{-0.04}$	23.12 <sup>f</sup>	
GOODSS087	J033218.24-275241.4	2.801	$1.00^{+0.14}_{-0.15}$	$43.76^{+0.07}_{-0.06}$	23.32 <sup>f</sup>	BLAGN
GOODSS089	J033208.27-274153.5	2.470	$1.27^{+0.18}_{-0.20}$	$43.73^{+0.07}_{-0.06}$	N.A.	BLAGN
GOODSS091	J033242.84-274702.5	3.193	$2.32^{+0.20}_{-0.21}$	$44.27^{+0.04}_{-0.04}$	23.59 <sup>f</sup>	BLAGN
GOODSS094	J033244.01-274635.0	2.688	$1.14^{+0.12}_{-0.13}$	$43.77^{+0.05}_{-0.05}$	22.58 <sup>f</sup>	
GOODSS117	J033203.04-274450.1	2.573	$1.61^{+0.17}_{-0.18}$	$43.87^{+0.05}_{-0.05}$	22.33	
GOODSS202	J033229.85-275105.9	3.700	$3.44^{+0.31}_{-0.34}$	$44.61^{+0.04}_{-0.04}$	22.50 <sup>f</sup>	
GOODSS263	J033218.83-275135.5	3.660	$1.46^{+0.27}_{-0.32}$	$44.22^{+0.09}_{-0.09}$	22.38 <sup>f</sup>	
GOODSS642	J033215.18-274158.7	2.402	$0.85^{+0.15}_{-0.15}$	$43.52^{+0.08}_{-0.07}$	22.18 <sup>f</sup>	
GOODSS901	J033235.71-274916.0	2.578	$0.78^{+0.16}_{-0.20}$	$43.56^{+0.10}_{-0.10}$	21.75 <sup>f</sup>	

<sup>a</sup>0.5–8 keV flux from Alexandar et al. (2003) in unit of  $1 \times 10^{-15}$  erg s<sup>-1</sup> cm<sup>-2</sup>.

<sup>b</sup>2–10 keV hard X-ray luminosity. It is calculated with the 0.5–8 keV flux and the photon index of the best fit power-law model in the 0.5–8 keV band from Alexandar et al. (2003).

<sup>c</sup> $K_{AB}$  magnitude. For GOODSN objects,  $K_{AB}$  band magnitudes are derived from corrected-aperture  $HK'_{\text{vega}}$  band magnitude with  $HK'_{\text{vega}} - K_{\text{vega}} = 0.13 + 0.05(I_{\text{vega}} - K_{\text{vega}})$  (Barger et al. 2003) and  $K_{AB} - K_{\text{vega}} = 1.83$ . For GOODSS objects, the  $K_{AB}$ -band magnitudes are mostly measured on the ISSAC deep  $K$ -band image of the GOODSS field (Vandame et al. (2004) in preparation). We use the AUTO magnitude with SExtractor in AB magnitude system. “I” indicates that the magnitude is taken from the mosaiced ISSAC image. Remaining 4 objects,  $K_{AB}$  magnitudes are taken from Szokoly et al. (2003). Vega magnitude in Szokoly et al. (2003) are converted to AB magnitude with the conversion above. N.A. means  $K_{AB}$  magnitude is not available for the object.

<sup>d</sup>BLAGN indicates an AGN with broad emission line in the optical wavelength.

<sup>e</sup>Redshift from Dawson et al. (2003)

for objects at below the redshifts, the central wavelength of the  $K$ -band corresponds to the wavelength range above  $4000\text{\AA}$  break in the object frame. There are 14 (GOODSN) and 17 (GOODSS) AGNs with spectroscopic redshifts between  $2 < z_{\text{sp}} < 4$  in the region covered with the ACS imaging surveys in GOODS fields (Table 1). The  $0.5\text{--}8\text{ keV}$  X-ray fluxes taken from Alexander et al. (2003), and  $L_{2\text{--}10\text{keV}}$  of the objects are listed in the table. The  $L_{2\text{--}10\text{keV}}$  is calculated from the  $0.5\text{--}8\text{ keV}$  flux and the best fit photon index in the  $0.5\text{--}8\text{ keV}$  band by Alexander et al. (2003). The  $L_{2\text{--}10\text{keV}}$  of the sample ranges from  $10^{43.5}\text{ erg s}^{-1}$  to  $10^{45.0}\text{ erg s}^{-1}$ .

The sample is not complete as X-ray flux limited AGNs at  $2 < z_{\text{sp}} < 4$ , because the optical identification of the X-ray sources in both of the GOODSN and GOODSS fields is not complete. In GOODSN (GOODSS) area, the completeness of the spectroscopic identification is 56% (40%) in total and 87% (78%) for objects brighter than  $R = 24$  (Barger et al. 2003; Szokoly et al. 2003). The photometric redshift estimation by Barger et al. (2003) implies that there can be the same number of objects with only photometric redshift as the spectroscopically-identified objects at  $2 < z < 4$ . We miss some objects with fainter optical magnitudes, which correspond to smaller star-formation rates and stellar masses, than those of AGNs with  $z_{\text{sp}}$  on average.

We examine the photometric properties of the host galaxies of the AGNs at  $2 < z_{\text{sp}} < 4$  with the ACS GOODS Ver 0.5 images in the optical wavelength (Giavalisco et al. 2004). Their F775W-band images are shown in Figure 1. The pixel scale of the ACS image is  $0.''03\text{ pixel}^{-1}$  after the ‘‘drizzle’’ data reduction procedure (Fruchter & Hook 2002). All of the AGNs at  $2 < z_{\text{sp}} < 4$  are detected in the GOODS Ver 1.0 catalogs made by the GOODS team<sup>2</sup>. The catalogs are made by applying SExtractor object detection algorithm (Bertin & Arnouts, 1996) to the F435W, F606W, F775W, and F850LP-band images. We use all bands but F435W in this study, because the F435W magnitudes are affected by absorption blue-ward of  $\text{Ly}\alpha$  for most of the AGNs at  $2 < z_{\text{sp}} < 4$ . AUTO magnitudes, aperture magnitudes, and CLASS\_STAR stellarities of the objects used in the following sections are from the catalog. In addition to the magnitudes, a total magnitude of each AGN is determined by applying aperture photometry to the GOODS Ver 0.5 images. The aperture is determined for each object independently to cover the whole extended structure. The sky level is determined so as to keep the the total counts at large aperture radii ( $\sim 10\text{ FWHM}$ ) to a constant value. Some of the objects have a close companion around them, for example GOODSS091. We include the contribution from the companion object(s) in the photometric measurements below if the object is within  $0.''5$  ( $\sim 5\text{ kpc}$ ) from the primary object.

We use  $K_{\text{AB}}$ -band magnitudes of the AGNs for estimations of the stellar masses of the host galaxies. The  $K_{\text{AB}}$ -band magnitudes of the AGNs are listed in Table 1. For all objects in GOODSN fields, the  $K_{\text{AB}}$ -band magnitudes are derived from corrected-aperture  $HK'_{\text{vega}}$  band magnitude with  $HK'_{\text{vega}} - K_{\text{vega}} = 0.13 + 0.05(I_{\text{vega}} - K_{\text{vega}})$  (Barger et al. 1999) and  $K_{\text{AB}} - K_{\text{vega}} = 1.83$ . For 12 GOODSS AGNs, the  $K_{\text{AB}}$ -band magnitudes are measured from ISAAC (Infrared Spectrometer And Array Camera) deep  $K_s$ -band image of the GOODSS field (Vandame et al. 2004, in preparation). The ISAAC observations have been carried out using the Very Large Telescope at the ESO Paranal Observatory under Pro-

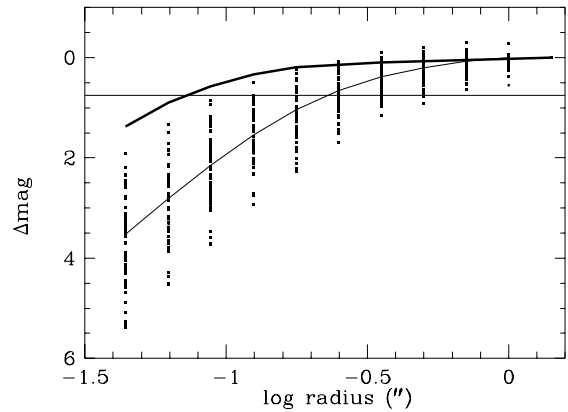


FIG. 2.— Average growth curves of the 400 stellar objects (thick solid line) and 55 galaxies at  $2 < z_{\text{sp}} < 4$  (thin solid line) in the F775W band. Growth curves of the individual galaxies at  $2 < z_{\text{sp}} < 4$  are plotted with filled squares. All of the profiles are normalized at  $1.''4$  radius. The horizontal line indicates  $0.75\text{mag}$  difference, i.e. half light.

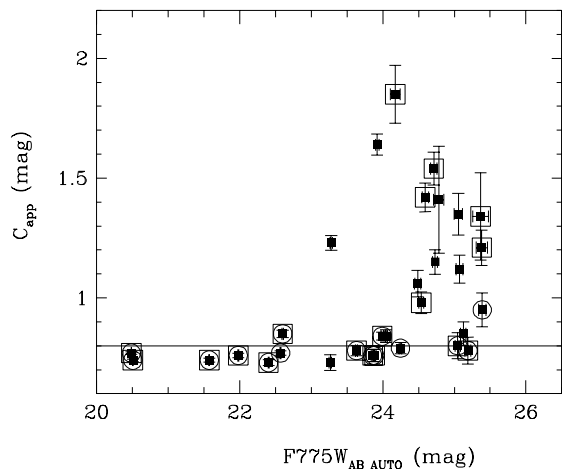


FIG. 3.— Concentration parameters and AUTO magnitudes of AGNs at  $2 < z_{\text{sp}} < 4$  in the F775W band. The open circles indicate AGNs with a broad-line in their optical spectra. The ‘‘stars’’ have  $C_{\text{app}}$  smaller than the stellerity limit shown with the solid line,  $C_{\text{app}} = 0.8$  in the band. The large open circles and open squares indicate AGNs with broad emission line in their optical spectra and with  $L_{2\text{--}10\text{keV}} > 10^{44}\text{ erg s}^{-1}$ , respectively.

gram ID:LP168.A-0485. We apply SExtractor source detection to the images with a magnitude zero-point of 26.0 mag and use the AUTO magnitudes. Other 4 GOODSS AGNs,  $K_{\text{AB}}$ -band magnitudes are taken from Szokoly et al. (2003). Vega magnitudes in Szokoly et al. (2003) are converted to AB magnitudes with the same conversion above. Remaining one object (GOODSS089) is covered in neither of the data.

### 3. PHOTOMETRIC PROPERTIES OF THE HOST GALAXIES OF THE HIGH- $Z$ AGNS

#### 3.1. Concentration Parameters of the Images of the High- $z$ AGNs

We examine the concentration parameters of the images of each object in F606W, F775W, and F850LP bands, in order to divide the high- $z$  AGNs into two samples; AGNs dominated by PSF component without a significant extended component (‘‘compact’’ AGNs), and AGNs with an extended component (‘‘extended’’ AGNs). We adopt a concentration parameter derived from the difference of aperture magnitudes at two radii,

<sup>2</sup> Available from <http://www.stsci.edu/science/goods/>

TABLE 2  
 AUTO MAGNITUDES AND CONCENTRATION PARAMETERS OF THE AGN IMAGES

Name	Auto Mag. <sup>a</sup>			$C_{\text{app}}$ <sup>b</sup>		
	F606W <sub>AB</sub>	F775W <sub>AB</sub>	F850LP <sub>AB</sub>	F606W <sub>AB</sub>	F775W <sub>AB</sub>	F850LP <sub>AB</sub>
GOODSN052	22.71 ± 0.01	22.57 ± 0.01	22.62 ± 0.01	0.74 ± 0.01	0.77 ± 0.01	0.91 ± 0.01
GOODSN077	23.38 ± 0.01	23.27 ± 0.02	23.13 ± 0.02	0.75 ± 0.02	0.73 ± 0.03	0.92 ± 0.03
GOODSN137	20.49 ± 0.01	20.51 ± 0.01	20.27 ± 0.01	0.74 ± 0.00	0.74 ± 0.01	0.88 ± 0.00
GOODSN161	24.62 ± 0.02	23.89 ± 0.02	23.70 ± 0.02	0.69 ± 0.02	0.76 ± 0.03	0.88 ± 0.02
GOODSN176	25.26 ± 0.03	25.05 ± 0.04	25.15 ± 0.05	0.77 ± 0.04	0.80 ± 0.05	1.01 ± 0.06
GOODSN190	23.75 ± 0.01	23.28 ± 0.02	22.91 ± 0.02	1.13 ± 0.02	1.23 ± 0.03	1.39 ± 0.03
GOODSN330	25.30 ± 0.03	25.13 ± 0.04	25.07 ± 0.04	0.83 ± 0.04	0.85 ± 0.05	1.06 ± 0.05
GOODSN377	24.31 ± 0.02	23.92 ± 0.03	23.57 ± 0.02	1.68 ± 0.03	1.64 ± 0.04	1.71 ± 0.04
GOODSN394	22.83 ± 0.01	22.60 ± 0.01	22.29 ± 0.01	0.85 ± 0.01	0.85 ± 0.02	0.98 ± 0.01
GOODSN398	24.84 ± 0.03	24.59 ± 0.05	24.42 ± 0.05	1.33 ± 0.04	1.42 ± 0.06	1.57 ± 0.06
GOODSN409	24.48 ± 0.01	24.04 ± 0.02	23.74 ± 0.02	0.84 ± 0.02	0.84 ± 0.03	0.99 ± 0.02
GOODSN411	23.96 ± 0.01	23.63 ± 0.01	23.62 ± 0.02	0.73 ± 0.02	0.78 ± 0.02	0.96 ± 0.02
GOODSN459	21.62 ± 0.01	21.58 ± 0.01	21.31 ± 0.01	0.70 ± 0.01	0.74 ± 0.01	0.87 ± 0.01
GOODSN478	22.47 ± 0.01	21.98 ± 0.01	21.87 ± 0.01	0.73 ± 0.01	0.76 ± 0.01	0.91 ± 0.01
GOODSS021	23.99 ± 0.01	23.86 ± 0.02	23.98 ± 0.02	0.71 ± 0.02	0.76 ± 0.03	0.89 ± 0.03
GOODSS024	22.89 ± 0.01	22.40 ± 0.01	22.43 ± 0.01	0.68 ± 0.01	0.73 ± 0.01	0.84 ± 0.01
GOODSS027	25.53 ± 0.05	24.71 ± 0.05	24.55 ± 0.05	1.46 ± 0.07	1.54 ± 0.07	1.66 ± 0.07
GOODSS045	25.87 ± 0.09	25.37 ± 0.11	24.83 ± 0.08	1.41 ± 0.15	1.34 ± 0.18	1.84 ± 0.17
GOODSS057	24.13 ± 0.03	24.17 ± 0.07	23.76 ± 0.19	1.84 ± 0.07	1.85 ± 0.12	1.96 ± 0.17
GOODSS062	20.80 ± 0.01	20.49 ± 0.01	20.31 ± 0.01	0.72 ± 0.00	0.77 ± 0.00	0.89 ± 0.00
GOODSS068	24.14 ± 0.01	23.99 ± 0.01	23.78 ± 0.02	0.79 ± 0.01	0.84 ± 0.02	0.95 ± 0.02
GOODSS085	25.16 ± 0.02	24.73 ± 0.03	24.61 ± 0.03	1.05 ± 0.04	1.15 ± 0.05	1.32 ± 0.05
GOODSS087	24.37 ± 0.01	24.25 ± 0.02	24.28 ± 0.02	0.73 ± 0.02	0.79 ± 0.02	0.93 ± 0.03
GOODSS089	25.49 ± 0.03	25.39 ± 0.05	25.14 ± 0.05	0.84 ± 0.04	0.95 ± 0.07	1.08 ± 0.07
GOODSS091	25.04 ± 0.02	25.19 ± 0.04	25.18 ± 0.04	0.75 ± 0.03	0.78 ± 0.06	0.89 ± 0.06
GOODSS094	24.64 ± 0.02	24.49 ± 0.04	24.37 ± 0.04	1.07 ± 0.04	1.06 ± 0.05	1.23 ± 0.06
GOODSS117	25.80 ± 0.05	25.07 ± 0.05	24.70 ± 0.04	1.13 ± 0.06	1.12 ± 0.06	1.23 ± 0.05
GOODSS202	25.18 ± 0.03	24.54 ± 0.03	24.64 ± 0.05	0.80 ± 0.04	0.98 ± 0.05	1.34 ± 0.06
GOODSS263	25.67 ± 0.05	25.38 ± 0.08	25.09 ± 0.08	1.24 ± 0.06	1.21 ± 0.07	1.67 ± 0.10
GOODSS642	25.60 ± 0.05	25.06 ± 0.06	24.85 ± 0.06	1.25 ± 0.07	1.35 ± 0.09	1.68 ± 0.08
GOODSS901	25.37 ± 0.06	24.78 ± 0.07	24.66 ± 0.08	1.01 ± 0.15	1.41 ± 0.22	1.49 ± 0.23

<sup>a</sup>AUTO magnitude from GOODS catalog version 1.0.

<sup>b</sup>Concentration parameter derived with  $C_{\text{app}} \equiv \text{mag}_{\text{app}}(< 0.''07) - \text{mag}_{\text{app}}(< 0.''25)$ .

following Abraham et al. (1994). We choose the inner radius so as to match the size of the PSF and outer radius to match the typical size of galaxies at  $2 < z_{\text{sp}} < 4$  the same redshift range as the AGNs.

The radial profile of the PSF is determined by the average profile of “stars” selected in the following way from the ACS images. First, we choose objects whose SExtractor stellarity parameters, CLASS\_STAR, in all of the F606W, F775W, and F850LP bands are larger than 0.95 in the magnitude range  $21 < m_{\text{F775W}} < 26$  mag. In the magnitude range “stars” form a clear sequence with CLASS\_STAR around 0.98 in the magnitude vs. CLASS\_STAR diagram, thus “stars” can be clearly separated from extended objects using the threshold, which enclose the outer envelop of the sequence. The magnitude range covers slightly fainter than that of the  $2 < z_{\text{sp}} < 4$  AGN sample (i.e.  $20.5 < m_{\text{F775W}} < 25.4$ ). Then, we check the images of the “stars” by eye and remove objects affected by nearby bright objects, edge of the field of view, and residual of bad pixels and cosmic-rays. About 20% of the objects are rejected, and 205 and 195 stars are remained in the GOODSN and the GOODSS fields, respectively.

The profiles of galaxies are examined using the galaxies at  $2 < z_{\text{sp}} < 4$  selected from the compiled redshift survey catalogs in the GOODSN field (Cohen et al. 2000; Cowie et al. 2004). There are 55 galaxies in the redshift range within the area covered by the ACS imaging, excluding the objects detected by *Chandra*. The magnitudes of the 55 galaxies are distributed between  $22 < m_{\text{F775W}} < 27$  mag.

The half-light radii of the average profiles are measured to be  $0.''08$  (2.6 pixel) for the “stars” and  $0.''23$  (7.7 pixel) for the  $2 < z_{\text{sp}} < 4$  galaxies from the average growth curves shown in Figure 2 with thick solid line and thin solid line, respectively. The half-light radius is consistent with that measured in the bright U-dropout LBG sample (Bouwens, Broadhurst, & Illingworth 2003). Based on the results, from aperture magnitudes available in the GOODS Ver. 1.0 catalog, we choose those with radii of  $0.''07$  (2.08 pixel) and  $0.''25$  (8.34 pixel), and define the concentration parameter as  $C_{\text{app}} = \text{mag}_{\text{app}}(< 0.''07) - \text{mag}_{\text{app}}(< 0.''25)$ . It should be noted that a stellar object has a smaller  $C_{\text{app}}$  than an extended object. We use the concentration parameter instead of the CLASS\_STAR, which is derived by a neural network method with isophotal areas, to evaluate the stellarity of an object. Because we can more simply estimate the uncertainty for the stellarity using the concentration parameter than using the CLASS\_STAR.

The distribution of  $C_{\text{app}}$  of the “stars” does not change significantly in the magnitude range of the “stars”. Based on the cumulative distributions of  $C_{\text{app}}$ , we decide to regard an object with the  $C_{\text{app}}$  smaller than 0.79, 0.80, and 0.96 in the F606W, F775W, and F850LP bands, respectively, as a stellar object. Ninety-five percent of the “stars” fall below the stellarity limits. The  $C_{\text{app}}$  of the AGNs at  $2 < z_{\text{sp}} < 4$  are summarized in Table 2 along with the AUTO magnitudes.

Based on the  $C_{\text{app}}$  of the F606W, F775W, and F850LP images, we divide the sample of the AGNs at  $2 < z_{\text{sp}} < 4$  into “extended” and “compact” AGNs. Seventeen  $2 < z_{\text{sp}} < 4$

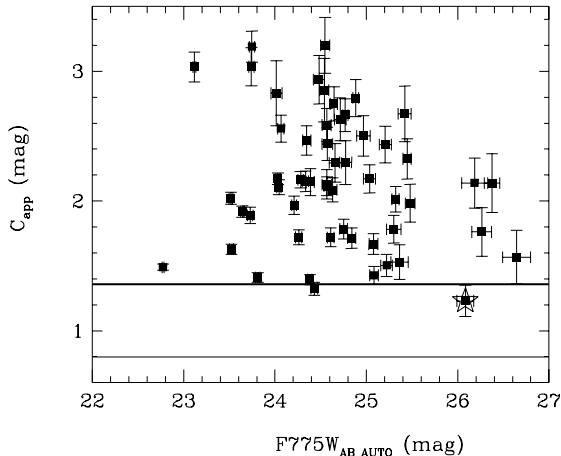


FIG. 4.— Concentration parameters and AUTO magnitudes of the  $55 < z_{\text{sp}} < 4$  galaxies in the F775W band. The thick solid line represents the  $C_{\text{app}}$  value of a  $z = 3$  object with the de Vaucouleurs profile with effective radius of 1 kpc and axis ratio of 0.4, which represents the most concentrated host galaxies observed in the nearby universe (e.g., Schade et al. 2000). The solid line shows the stellarity limit. The open star indicates the most concentrated faint object used as the upper limit for GOODS N176 and GOODSS091, see Section 3.2 for details.

AGNs have concentration parameters larger than the stellarity limits in all of the F606W, F775W, and F850LP band images. Hereafter, we call them “extended” AGNs. Remaining 14 AGNs are not significantly extended at least in one of the three bands (“compact” AGN). Because we use the criteria that the “extended” AGNs are significantly extended in all of the three bands, we expect the number of the contamination of purely point-like source to the “extended” sample is negligible. On the contrary, the “compact” sample can have objects with faint extended components in one band.

In Figure 3, the F775W band  $C_{\text{app}}$  of the AGNs are plotted against their F775W band AUTO magnitudes. The large open circles in the figure indicate the objects that show a broad-emission line in their optical spectra. They tend to have smaller  $C_{\text{app}}$ , which means they show a stellar image. The large open squares indicate AGNs with  $L_X > 10^{44}$  erg  $\text{s}^{-1}$ . There is no clear correlation between the hard X-ray luminosity of the AGN and the  $C_{\text{app}}$ .

### 3.2. Upper Limits on the Brightnesses of the Host Galaxies of the “Compact” AGNs

Due to the bright nuclear stellar components of the “compact” AGNs, it is impossible to directly estimate the brightnesses of their host galaxies. We can only determine the upper limits of the brightnesses of the host galaxies of the “compact” AGNs. We compare the  $C_{\text{app}}$  of the AGNs with those of simulated images, which consist of a stellar nuclear component and an extended host galaxy component. If the stellar component dominates a simulated image, the  $C_{\text{app}}$  of the simulated image should be close to that of the image of a “compact” AGN. The contribution from the extended component increases, the  $C_{\text{app}}$  of the simulated images increases, and at some points, the  $C_{\text{app}}$  exceeds the observed upper limits. We use the brightness of the extended component with which the  $C_{\text{app}}$  of the simulated image exceed the observed  $C_{\text{app}}$  value as the upper limit of the brightness of the host galaxy. We assume that the nuclear component comes from the AGN component, not from a nuclear star-burst component.

The simulated images are constructed by adding the images of stars to the images of high-redshift galaxies. Because we do not have information on the morphological distribution of high-redshift galaxies, we do not make model galaxy image with typical galaxy profiles, such as the de Vaucouleurs profile, observed in the nearby universe. As the model host galaxy images, we use the images of high-redshift field (non-AGN) galaxies in the GOODS fields themselves, i.e. the  $55 < z_{\text{sp}} < 4$  galaxies selected in Section 3.1. It should be noted that the upper limit evaluation can be affected by morphological distribution of the model host galaxies. If the host galaxies of the AGNs are systematically more concentrated than the field galaxies, the estimated upper limits can be fainter than the real host galaxy brightness. The magnitudes and the concentration parameters of the  $55 < z_{\text{sp}} < 4$  galaxy are shown in Figure 4. They cover quite large range of the  $C_{\text{app}}$  value, and the most concentrated objects are as concentrated as an  $z = 3$  object with the de Vaucouleurs profile with effective radius of 1 kpc and axis ratio of 0.4 ( $C_{\text{app}}$  of 1.47). The profile represents the most concentrated host galaxies observed in the nearby universe (e.g., Shade et al. 2000). Thus, the assumption that the  $2 < z_{\text{sp}} < 4$  galaxy sample covers the morphologies of the most concentrated AGN host galaxies is acceptable.

For the “star” sample, we select from from the 400 “stars” used in Section 3.1. We only use “stars” in the magnitude range between the magnitude of the brightest “compact” AGN (GOODSN137) and one magnitude fainter than that for the simulation. There are 19, 38, and 53 “stars” in the magnitude range in the F606W, F775W, and F850LP bands. We normalize the image of a star so that the total magnitude of the simulated image match the observed magnitude of each AGN. For each “compact” AGN,  $19 \times 55 = 1045$  (F606W),  $38 \times 55 = 2090$  (F775W), and  $53 \times 55 = 2915$  (F850LP) simulated images are typically made. We do not change the normalization of the model galaxy image, in order to escape from changing of the signal-to-noise ratio of the simulated images. Thus, for the two faint “compact” AGNs, GOODSN176 and GOODSS091, only  $2 < z_{\text{sp}} < 4$  galaxies fainter than the AGNs are used for the simulation.

The distribution of the measured  $C_{\text{app}}$  of the simulated images and the magnitudes of the model galaxy components used in the image is shown in Figure 5 for the F775W-band case. Each dot represents a simulated image. A simulated image made with a brighter model galaxy component have larger  $C_{\text{app}}$  on average than that with a fainter galaxy component as expected. The scatter in the vertical direction at a certain magnitude is owing to the difference of the “star” images used in the simulations. The scatter represents the effect of the PSF variation in the field of view.

The horizontal solid lines in each panel indicate the concentration parameter of each AGN and  $1 \sigma$  range. We use the magnitude of the brightest  $2 < z_{\text{sp}} < 4$  galaxy with which the simulated image with the smallest concentration parameter exceed the  $1 \sigma$  upper limit of the observed  $C_{\text{app}}$  value as the upper limits of the brightnesses of the host galaxies. The resulting upper limits on the brightnesses of the host galaxies are summarized in “upper limit” column of Table 4. For GOODSN176 and GOODSS091, even the simulated image with the faintest model galaxy exceeds their upper limits of  $C_{\text{app}}$ . We use the magnitude of the most concentrated faint object in the  $55 < z_{\text{sp}} < 4$  galaxies (indicated with open star in Figure 4) as their upper limits. The nucleus of GOODSN137 and GOODSS062 are too bright to determine useful upper

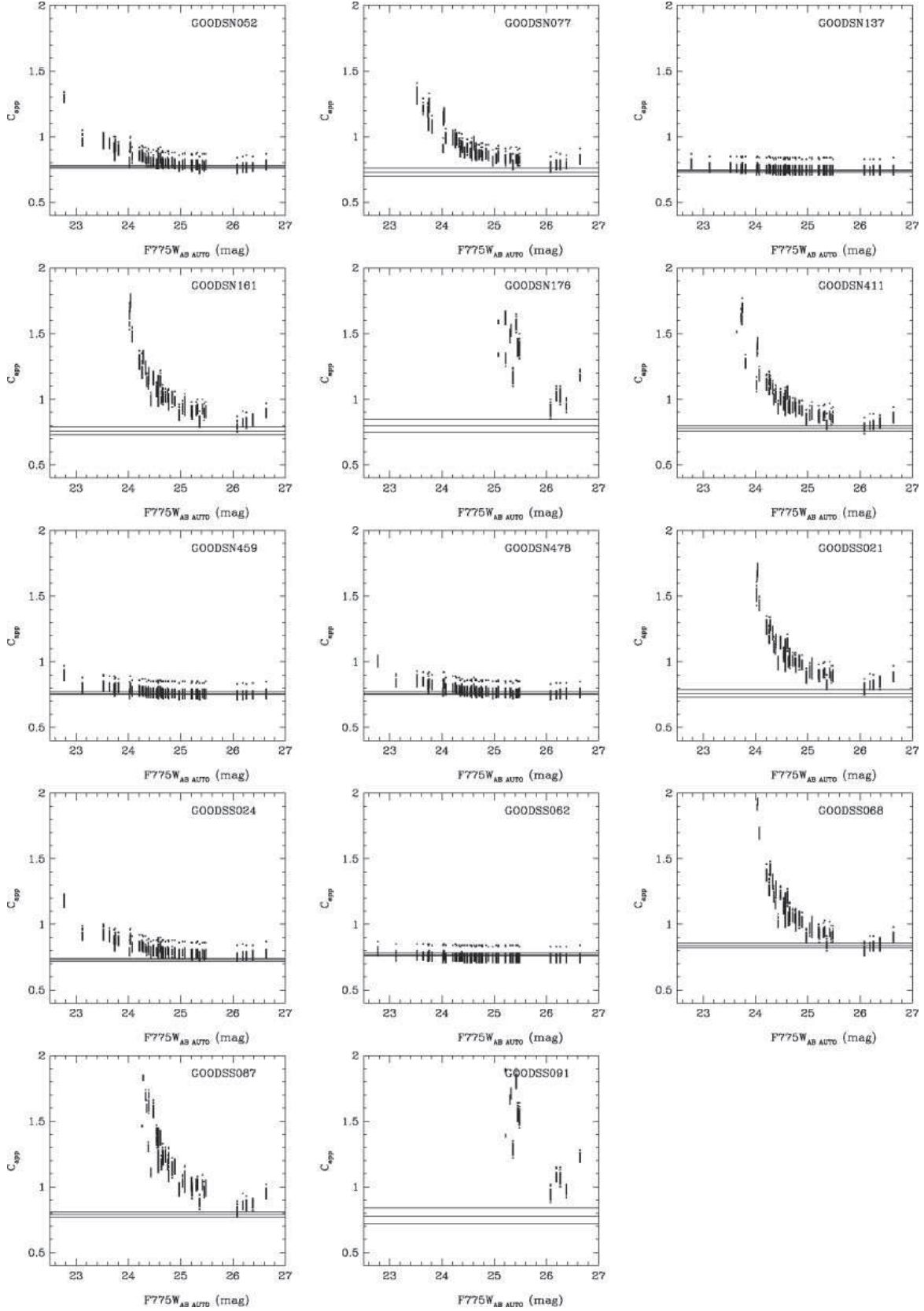


FIG. 5.— The distributions of the  $C_{app}$  parameters of the simulated images and the magnitudes of the model galaxy component used in the simulated images. A dot represent a result with a simulated image. Each panel corresponds to an “compact” AGN. Horizontal lines in each panel represent the  $1\sigma$  range of the  $C_{app}$  of the AGN.

limits of the brightnesses of their host galaxies. We remove the two objects from discussions below.

We expect that the uncertainty on the upper limits are less than 0.5 mag, based on the number of the most concentrated galaxies in the  $2 < z_{\text{sp}} < 4$  galaxies (about 1 per 0.5 mag bin, see Figure 4). Because we do not know the morphological distribution of the AGN host galaxies at high redshifts, especially as a function of magnitude, it is impossible to rigidly estimate the uncertainty of the upper limits.

### 3.3. Upper and Lower Limits on the Brightness of the Host Galaxies of the “Extended” AGNs

Even for the “extended” AGNs, it is still difficult to directly evaluate the brightness of the host galaxy by fitting the nuclear and the host galaxy components to the 2-dimensional images of the AGN. Therefore, we robustly estimate the upper and lower limits of their brightness as follows.

We use the total magnitudes of the “extended” AGNs as the upper limits of the brightnesses of the host galaxies. The total magnitude of an AGN include the host galaxy component and the nuclear component, thus the magnitude of the host galaxy has to be fainter than the total magnitude. The total magnitudes of the “extended” AGNs are listed in Table 3.

We evaluate the lower limit of the brightness of the host galaxy by subtracting the maximal PSF contribution whose central surface brightness matches the peak surface brightness of the total image. Because the central surface brightness of the nuclear component can not exceed the peak surface brightness of the total image. We use the aperture magnitudes within a  $0.''04$  (1.46 pixel) radius as the peak surface brightness. The average profile of the “stars” (Figure 2) is used as the average PSF radial profile.

The profile of each “star” can be different from the average profile of the “stars”, due to a PSF variation across the field of view and an insufficient signal-to-noise ratio. For the 400 “stars” selected in Section 3.1, the total magnitude estimated from the aperture magnitude is consistent with the measured total magnitude within  $\pm 0.2$  mag with systematic offset less than 0.05 mag. Therefore for the “extended” AGNs, we can regard the magnitude difference over 0.2 mag as the significant difference between the total magnitude and the maximal PSF contribution of the nuclear component.

The magnitude differences between the total magnitudes and the maximal PSF contributions for the “extended” AGNs are shown in Figure 6 with filled squares as a function of the total magnitudes. All of the “extended” AGNs, except for GOODS330 and GOODS409, have magnitude difference larger than 0.2 mag. We evaluate lower limit of the brightness of the host galaxy with the residual flux after subtracting the maximal PSF contribution from the total magnitude. The resulting lower limits are shown in column “Lower Limits” in Table 3.

The uncertainty of the lower limit consists of the uncertainties of the  $0.''04$  aperture magnitude, the total magnitude, and the profile of the PSF, i.e. conversion factor from the  $0.''04$  aperture magnitude to the maximal PSF contribution. The  $\pm 0.2$  mag dispersion in the conversion factor mentioned in the previous paragraph dominates the uncertainty of the lower limits estimations in most of the cases. The estimated uncertainties are listed in Table 3. For GOODS330 and GOODS409, the magnitude differences between the total magnitudes and the maximal PSF contributions are less than 0.2 mag, thus we cannot determine their lower uncertainty of the lower limits (shown with +9.99 in Table 3).

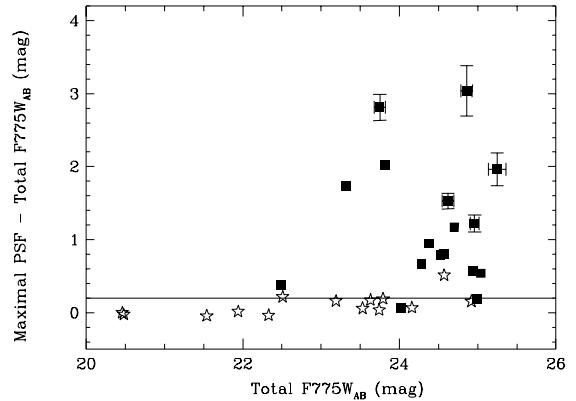


FIG. 6.— Differences between the total F775W-band magnitudes and the maximal PSF contributions in the band of “extended” (filled square) and the “compact” (open star) AGNs as a function of the total magnitudes. Only error bar that is significantly larger than each point is shown. The horizontal solid line show the upper envelop of the distribution of the differences of the “stars”.

For comparison, the “compact” AGNs are also plotted in the same figure with the star marks. All but GOODS176 have the magnitude difference of less than 0.2 mag which is consistent with being the stellar image. GOODS176 has magnitude difference of 0.51 mag in the F775W-band and consistent with the  $C_{\text{app}}$  value of 0.80 which is close to the stellarity threshold value in the band. Because the object has  $C_{\text{app}}$  value less than stellarity threshold in the F606W-band, it is classified as a “compact” AGN.

## 4. RESULTS

### 4.1. Absolute UV Magnitudes of the Host Galaxies

Using the upper and lower limits of the brightnesses of the host galaxy in the F606W and F775W bands, we derive the limits on their UV absolute magnitudes,  $M_{\text{AB}1700}$ . We interpolate or extrapolate the brightness limits in the two bands to derive the limits at object-frame  $1700\text{\AA}$ . The derived absolute magnitude limits are shown in Figure 7 against  $L_{2-10\text{keV}}$ . The upper limits of the “compact” AGNs are distributed from  $M_{\text{AB}1700} = -19.0$  to  $M_{\text{AB}1700} = -21.5$  (left panel). The lower and upper limits of the “extended” AGNs are distributed from  $M_{\text{AB}1700} = -17.0$  to  $M_{\text{AB}1700} = -22.5$  (right panel). The knee of the UV luminosity function ( $L^*$ ) of LBGs at  $z \sim 3$  is  $M_{\text{AB}1700} = -21.2$  mag (Steidel et al. 1999), thus the limits on the host galaxies correspond to  $0.02L^* - 3L^*$ . There is no clear difference between the upper limits on the luminosities of the host galaxies of the “compact” and “extended” AGNs.

If we assume that star formation in the host galaxies is continuous at the time of the observation, their UV luminosities reflect the star formation rates of the host galaxies. The star formation rate can be derived from UV luminosity with  $SFR = 1.3(2.9) \times 10^{-28} L_{\nu}(\lambda 1500)$  erg  $\text{s}^{-1} \text{Hz}^{-1}$  (Madau, Pozzetti, & Dickinson 1998) with Salpeter (Scalo) initial mass function (IMF). The derived SFR with Salpeter IMF without extinction correction is shown in the top horizontal axis of Figure 7. The limits of the UV absolute magnitudes of the host galaxies correspond to SFR of  $0.3 - 40 M_{\odot} \text{yr}^{-1}$ . The modest SFR is similar to the SFRs observed in the host galaxies of optically-selected moderate luminosity QSOs at  $1.8 < z < 2.75$  in the GEMS field overlapping the GOODSS region (Jahnke et al. 2004).

TABLE 3  
UPPER AND LOWER LIMITS ON THE BRIGHTNESSES OF THE HOST GALAXIES OF THE  
“EXTENDED” AGNS

Name	Total Mag. (Upper Limit) <sup>a</sup>			Lower Limit <sup>b</sup>		
	F606W <sub>AB</sub>	F775W <sub>AB</sub>	F850LP <sub>AB</sub>	F606W <sub>AB</sub>	F775W <sub>AB</sub>	F850LP <sub>AB</sub>
GOODSN190	23.70 ± 0.01	23.31 ± 0.02	22.98 ± 0.01	23.99 <sup>+0.07</sup> <sub>-0.05</sub>	23.56 <sup>+0.06</sup> <sub>-0.05</sub>	23.23 <sup>+0.06</sup> <sub>-0.05</sub>
GOODSN330	25.14 ± 0.03	24.99 ± 0.04	24.94 ± 0.04	26.84 <sup>+1.59</sup> <sub>-0.54</sub>	26.98 <sup>+9.99</sup> <sub>-0.69</sub>	27.13 <sup>+9.99</sup> <sub>-0.80</sub>
GOODSN377	24.26 ± 0.02	23.82 ± 0.03	23.54 ± 0.02	24.45 <sup>+0.05</sup> <sub>-0.05</sub>	24.00 <sup>+0.07</sup> <sub>-0.07</sub>	23.76 <sup>+0.06</sup> <sub>-0.06</sub>
GOODSN394	22.63 ± 0.01	22.48 ± 0.01	22.18 ± 0.01	23.77 <sup>+0.51</sup> <sub>-0.30</sub>	23.82 <sup>+0.73</sup> <sub>-0.37</sub>	23.90 <sup>+1.67</sup> <sub>-0.55</sub>
GOODSN398	24.69 ± 0.03	24.57 ± 0.04	24.03 ± 0.05	25.34 <sup>+0.20</sup> <sub>-0.14</sub>	25.27 <sup>+0.22</sup> <sub>-0.15</sub>	24.49 <sup>+0.12</sup> <sub>-0.09</sub>
GOODSN409	24.31 ± 0.01	24.02 ± 0.02	23.64 ± 0.02	26.09 <sup>+2.02</sup> <sub>-0.58</sub>	27.04 <sup>+9.99</sup> <sub>-1.38</sub>	26.62 <sup>+9.99</sup> <sub>-1.34</sub>
GOODSS027	25.49 ± 0.05	24.70 ± 0.05	24.45 ± 0.05	25.85 <sup>+0.10</sup> <sub>-0.10</sub>	25.15 <sup>+0.12</sup> <sub>-0.09</sub>	24.89 <sup>+0.12</sup> <sub>-0.09</sub>
GOODSS045	25.82 ± 0.09	25.25 ± 0.11	24.76 ± 0.08	26.01 <sup>+0.18</sup> <sub>-0.18</sub>	25.44 <sup>+0.22</sup> <sub>-0.22</sub>	24.92 <sup>+0.21</sup> <sub>-0.21</sub>
GOODSS057	23.89 ± 0.03	23.75 ± 0.07	23.84 ± 0.19	23.98 <sup>+0.18</sup> <sub>-0.10</sub>	23.83 <sup>+0.18</sup> <sub>-0.18</sub>	23.95 <sup>+0.30</sup> <sub>-0.30</sub>
GOODSS085	25.13 ± 0.02	24.52 ± 0.03	24.46 ± 0.03	26.15 <sup>+0.41</sup> <sub>-0.25</sub>	25.24 <sup>+0.23</sup> <sub>-0.16</sub>	25.30 <sup>+0.29</sup> <sub>-0.19</sub>
GOODSS089	25.41 ± 0.03	25.04 ± 0.05	25.01 ± 0.05	27.63 <sup>+9.99</sup> <sub>-0.82</sub>	26.06 <sup>+0.41</sup> <sub>-0.25</sub>	26.72 <sup>+1.63</sup> <sub>-0.54</sub>
GOODSS094	24.54 ± 0.02	24.38 ± 0.04	24.24 ± 0.04	25.10 <sup>+0.16</sup> <sub>-0.12</sub>	24.97 <sup>+0.17</sup> <sub>-0.12</sub>	24.74 <sup>+0.13</sup> <sub>-0.10</sub>
GOODSS117	25.49 ± 0.05	24.94 ± 0.05	24.42 ± 0.04	26.23 <sup>+0.24</sup> <sub>-0.17</sub>	25.91 <sup>+0.38</sup> <sub>-0.24</sub>	25.32 <sup>+0.33</sup> <sub>-0.21</sub>
GOODSS202	25.11 ± 0.03	24.28 ± 0.03	24.59 ± 0.05	26.91 <sup>+2.16</sup> <sub>-0.59</sub>	25.13 <sup>+0.30</sup> <sub>-0.20</sub>	25.45 <sup>+0.30</sup> <sub>-0.20</sub>
GOODSS263	25.28 ± 0.05	24.62 ± 0.08	24.92 ± 0.08	25.67 <sup>+0.10</sup> <sub>-0.08</sub>	24.92 <sup>+0.11</sup> <sub>-0.11</sub>	25.30 <sup>+0.13</sup> <sub>-0.13</sub>
GOODSS642	25.47 ± 0.05	24.96 ± 0.06	24.83 ± 0.06	25.91 <sup>+0.12</sup> <sub>-0.10</sub>	25.39 <sup>+0.11</sup> <sub>-0.11</sub>	25.38 <sup>+0.16</sup> <sub>-0.11</sub>
GOODSS901	25.04 ± 0.06	24.86 ± 0.07	24.48 ± 0.08	25.10 <sup>+0.21</sup> <sub>-0.21</sub>	24.93 <sup>+0.34</sup> <sub>-0.34</sub>	24.53 <sup>+0.40</sup> <sub>-0.40</sub>

<sup>a</sup>Total magnitude of the AGN derived from aperture photometry. See Section 2 for the details.

<sup>b</sup>The difference between the total magnitude and the maximal PSF contribution. +9.99 in the uncertainty of the lower limit represents no lower uncertainty is derived for the lower limit. See Section 3.3 for the details.

TABLE 4  
TOTAL MAGNITUDES AND UPPER LIMITS ON THE BRIGHTNESSES OF THE HOST GALAXIES OF  
THE “COMPACT” AGNS

Name	Total Mag. <sup>a</sup>			Upper Limit <sup>b</sup>		
	F606W <sub>AB</sub>	F775W <sub>AB</sub>	F850LP <sub>AB</sub>	F606W <sub>AB</sub>	F775W <sub>AB</sub>	F850LP <sub>AB</sub>
GOODSN052	22.64 ± 0.00	22.51 ± 0.01	22.50 ± 0.01	24.3	24.0	22.5
GOODSN077	23.34 ± 0.01	23.19 ± 0.02	23.04 ± 0.02	24.9	25.4	24.5
GOODSN137	20.46 ± 0.00	20.48 ± 0.00	20.22 ± 0.00	...	...	...
GOODSN161	24.49 ± 0.02	23.63 ± 0.02	23.48 ± 0.02	26.2	25.4	26.1
GOODSN176	25.13 ± 0.02	24.57 ± 0.04	24.97 ± 0.05	26.2	26.1	26.1
GOODSN411	23.91 ± 0.01	23.53 ± 0.01	23.45 ± 0.02	26.6	25.4	24.9
GOODSN459	21.57 ± 0.00	21.54 ± 0.00	21.24 ± 0.00	23.9	23.7	23.9
GOODSN478	22.41 ± 0.00	21.94 ± 0.01	21.79 ± 0.01	24.3	23.7	23.7
GOODSS021	23.92 ± 0.01	23.74 ± 0.02	23.88 ± 0.02	26.2	25.4	26.1
GOODSS024	22.83 ± 0.01	22.33 ± 0.01	22.35 ± 0.01	26.2	25.0	26.1
GOODSS062	20.77 ± 0.00	20.46 ± 0.00	20.26 ± 0.00	...	22.8	22.8
GOODSS068	23.95 ± 0.01	23.79 ± 0.01	23.55 ± 0.01	25.6	25.0	25.3
GOODSS087	24.19 ± 0.01	24.16 ± 0.02	24.14 ± 0.02	26.2	26.1	26.1
GOODSS091	24.92 ± 0.02	24.92 ± 0.04	25.07 ± 0.04	26.2	26.1	26.1

<sup>a</sup>Total magnitude of the AGN derived from aperture photometry. See Section 2 for the details.

<sup>b</sup>Upper limits of the brightness of the host galaxies. See Section 3.2 for the details.

## 4.2. Stellar Mass of the Host Galaxies

### 4.2.1. Stellar Mass Estimated from UV Luminosity, and the $M_{\text{bulge}} - M_{\bullet}$ relation

The stellar mass of a galaxy can be estimated with the UV luminosity. There is a loose correlation between observed  $M_{\text{AB}1700}$  and stellar mass of  $z \sim 3$  LBGs estimated by a SED (Spectral Energy Distribution) fitting (Papovich et al. 2001). For example an LBG with  $M_{\text{AB}1700} = -21$  mag, its stellar mass is estimated to be  $0.8 \times 10^{10} \sim 2.0 \times 10^{10} M_{\odot}$  on average. The scatter of the mass estimation comes from the different IMF and metallicity used in the SED fitting. It should be noted that there is one order of magnitude scatter in the stellar mass of each object from the average value.

On the other hand, the black hole mass of the nucleus can be estimated from the  $L_{2-10\text{keV}}$  with assumptions about  $L_{2-10\text{keV}}$  to bolometric luminosity ( $L_{\text{bol}}$ ) conversion factor (bolometric correction) and the Eddington ratio,  $\lambda$ . The bolometric correction of typical non-obscured QSOs is calculated to be  $\log(L_{\text{bol}}/L_{2-10\text{keV}}) = 1.54 + 0.24L' + 0.012L'^2 - 0.0015L'^3$ , where  $L' = \log(L_{\text{bol}}/10^{12})$  in unit of  $L_{\odot}$  by Marconi et al. (2004). With the bolometric correction and  $\lambda=1$ , an AGN with  $L_{2-10\text{keV}} = 10^{44} \text{ erg s}^{-1}$  is expected to have a bolometric luminosity of  $L_{\text{bol}} = 2.5 \times 10^{45} \text{ erg s}^{-1}$  and a black hole mass of  $2.7 \times 10^7 M_{\odot}$ .

The estimation of the black hole mass from the continuum luminosity of an AGN is plausible within a order of magni-

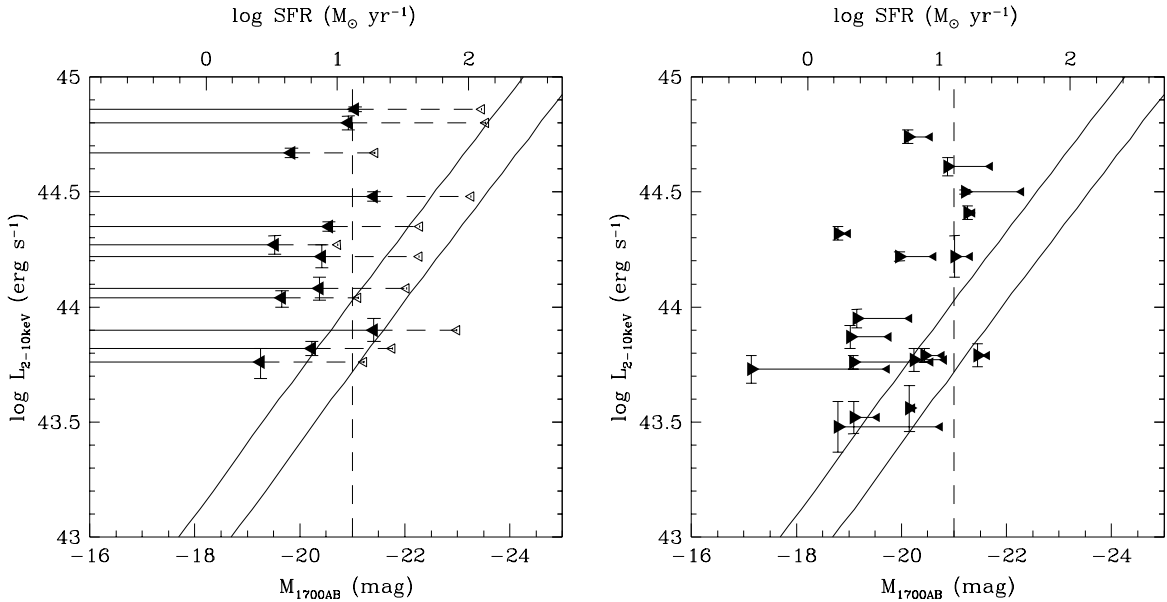


FIG. 7.— Left) Upper limits on the UV luminosity  $M_{\text{AB}1700}$  of the host galaxies of the “compact” AGNs (filled triangle) along with the total UV absolute magnitudes (open triangle). Right) Upper (small filled triangle) and lower (large filled triangle) limits on the UV luminosity of the host galaxies of the “extended” AGNs. In both panels, the horizontal solid lines represent the UV luminosity range allowed. The horizontal dashed lines in the left panel connect the upper limit with the total magnitude. The vertical dashed line indicates the knee of the UV luminosity function of  $z \sim 3$  LBGs (Steidel et al. 1999). The corresponding star-formation rate to the UV luminosity is shown in top horizontal axis. Two solid lines represents the relation between the spheroidal mass and the black hole mass in the local universe with the Eddington ratio ( $\lambda = 1$ ). The upper and lower lines represent the stellar mass estimations with  $0.8 \times 10^{10} M_{\odot}$  and  $2.0 \times 10^{10} M_{\odot}$  for  $M_{\text{AB}1700} = -21$  mag, respectively. See text for the details.

tude uncertainty. For optically-selected QSOs, there is a correlation between the continuum luminosity in the optical band and the black hole mass derived from the velocity width of a broad emission line and the continuum luminosity (Netzer 2003; Corbett et al. 2003; Warner, Hamann, & Dietrich 2003) with a dispersion of about 1 dex. Considering that the SEDs of non-obscured QSOs are similar to each other, we expect a correlation between the X-ray continuum luminosity and the black hole mass.

Using the stellar mass and the black hole mass estimations, we plot the  $M_{\text{bulge}} - M_{\bullet}$  relation found in the nearby galaxies ( $M_{\bullet}/M_{\text{bulge}} = 0.014$ ; Haring & Rix 2004) on Figure 7 for a case with  $\lambda = 1.0$ . We assume that the estimated stellar mass of the host galaxy represent that of the spheroidal component. The solid lines in Figure 7 represent the different stellar mass estimations for the same UV luminosity ( $0.8 \sim 2.0 \times 10^{10} M_{\odot}$  for  $M_{\text{AB}1700} = -21$  mag). Most of the upper limits on the luminosity of the host galaxy are distributed above the solid lines. This means, if we assume that the Eddington ratio does not exceed one, the  $M_{\text{bulge}} - M_{\bullet}$  relation in the local universe does not hold for the host galaxies of AGNs at high redshifts; the  $M_{\text{bulge}}$  of the host galaxies of the AGNs at high redshifts are smaller than those of nearby galaxies with the same  $M_{\bullet}$ . However, the estimated stellar masses from UV-luminosity is insecure, because the UV luminosity is dominated with bright early-type stars with small  $M/L$  ratio, and easily affected by dust extinction ( $A_{1700} = 9.65E(B-V)$ ; Calzetti et al. 2000).

#### 4.2.2. Stellar Mass Estimation with $K$ -band Magnitude for the “Extended” AGNs

The stellar mass of the host galaxy of the “extended” AGN is constrained better with its  $K_{\text{AB}}$  magnitude, which corresponds to the object-frame optical wavelength, than based only on the UV-luminosity. The stellar mass of the host galaxy

with the total  $K_{\text{AB}}$  magnitude is estimated as follows; first, we make models of galaxy SEDs with a stellar population synthesis code. Then we compare the models with the observed SEDs of the host galaxy, changing the normalization of the models, which is equivalent to changing the stellar mass of the model. We accept the SED models which do not exceed the upper and lower limits in all of the F606W, F775W, and F850LP bands. Finally, we select the SED models which are fainter than the observed  $K_{\text{AB}}$  magnitude from the accepted SED models, because the observed  $K_{\text{AB}}$  magnitude, which include the contribution from the nuclear component, is an upper limit on the host galaxy brightness. The range of the stellar masses of the selected models is the constraints on the stellar masses of the host galaxies. For the “compact” AGNs, we can not constrain the lower limits of the luminosity of the host galaxies, thus, the stellar mass estimation is applicable to only the “extended” AGNs. Since  $K_{\text{AB}}$ -band magnitude of GOODSS089 is not available, we remove the object in discussions below.

The SED models of galaxies are made by using PEGASE.2 stellar population synthesis code (Fioc & Rocca-Volmerange 1997). The host galaxies of QSOs observed in the nearby universe tend to be early-type galaxies (e.g., Dunlop et al. 2003), thus we made models of E and Sb type galaxies following the recipe in Kodama & Arimoto (1997;  $M_V = -22.49$ ) and Le Borgne & Rocca-Volmerange (2002), respectively. The star formation histories of E and Sb models roughly correspond to the instantaneous star formation and continuous star formation models, respectively.

The E type galaxy model parameters are determined so as to reproduce the optical color-magnitude relation of galaxies in the Coma cluster well (Kodama & Arimoto 1997). The star formation efficiency of  $3.33 \text{ Gyr}^{-1}$  and the infall time scale of 300 Myr are used. In the model, the galactic wind is intro-

duced at 0.39 Gyr and stops the star formation at that time. We use initial mass function (IMF) with a power of  $-1.2$  with the mass range of  $0.1 M_{\odot}$  to  $120 M_{\odot}$ .

The Sb type galaxy model parameters are chosen to reproduce the optical colors of Sb galaxies in the nearby universe (Le Borgne & Rocca-Volmerange 2002). The star formation efficiency of  $0.1 \text{ Gyr}^{-1}$  and the infall time scale of 8000 Myr are used. No galactic wind is introduced. Salpeter IMF with mass range of  $0.1 M_{\odot}$  to  $120 M_{\odot}$  is assumed.

The ages of the models are limited to be shorter than those of the universe at the redshift of each AGN. We use only models with ages longer than 100 Myr. The age step of the calculations is about one tenth of each age. In both of the E and Sb galaxy models, initial and infalling gas contains no metal ( $0.0 Z_{\odot}$ ). The metallicities of the stars and the gases are consistently calculated. The metallicities of the gas at the age of 5 Gyr exceed the solar metallicity in both of the models. The high metallicity of the gas component of the QSOs even at  $z = 2 \sim 4$  (for review, Hamann & Ferland 1999) is well reproduced with the E and Sb galaxy models. With the later-type galaxy recipes in Le Borgne & Rocca-Volmerange (2002), we cannot reproduce the high-metallicity of the QSOs. For the internal extinction, we do not use the model provided in the PEGASE.2 code, and apply the extinction curve for star-burst galaxies (Calzetti et al. 2000). We consider an extinction range of  $E(B-V) = 0.0 - 1.0$  mag which covers the range of  $E(B-V)$  estimated in  $z \sim 3$  LBGs ( $0.0 - 0.5$ ; Papovich et al. 2001; Shapley et al. 2001) with step of 0.1 mag.

We convert the model SEDs to the observed AB magnitudes at the redshift, using the filter and detector response functions of the ACS. We compare the model AB magnitudes with the upper and lower limits in F606W, F775W, and F850LP-bands by changing the normalization of the model. We only accept a model which do not exceed the upper limit, which is the  $1\sigma$  bright envelop of the total magnitude, and the lower limit, which is the lower envelop of the lower limits, all of the three bands simultaneously with a certain normalization. Because of the limited information, wide range of the SED models are acceptable. The example of the UV-constraints and the accepted models are shown in Figure 8. In this figure, we plot the accepted models with the largest stellar mass (thin solid curves; usually they have redder color, old and dust reddened stellar population with large mass-to-light ratio) and the smallest stellar mass (thin dashed curves; usually they have bluer color, young stellar population with small mass-to-light ratio) for each AGN along with the derived upper and lower limits in the optical bands.

For the accepted SED models and their normalizations, we calculate the  $K_{AB}$ -band magnitudes and stellar mass of the models. The distribution of the  $K_{AB}$  band magnitudes and the stellar masses of the accepted models for each object is shown in Figure 9. We select the accepted models whose  $K_{AB}$  band magnitudes are fainter than the observed  $K_{AB}$  magnitude. Because the  $K_{AB}$  magnitude includes the nuclear component, the host galaxy magnitude need to be fainter than the  $K_{AB}$  magnitude, which is shown with a horizontal thick solid line. Basically, accepted models with brighter  $K_{AB}$ -band magnitudes tend to have higher total mass. Thus the observed  $K_{AB}$ -band magnitude constrains the upper total mass of the galaxy. The selected model with the largest stellar mass is shown with the thick solid line in Figure 8. Finally, the stellar mass of the host galaxy can be constrained from the mass range of the selected models. The resulting stellar mass estimations are summarized in Table 5.

The resulting mass estimations are plotted in Figure 10 with triangles. The leftward filled triangles indicate the upper limits on the stellar mass, the rightward open triangles indicate the lower limits on the stellar mass. If we assume that the host galaxy component dominates the whole  $K_{AB}$ -band magnitude, the lower limit on the stellar mass becomes larger. The small rightward open triangles indicate the lower limits. The  $M_{\text{bulge}} - M_{\bullet}$  relation in the nearby universe ( $M_{\bullet}/M_{\text{bulge}} = 0.0014$ ; Haring & Rix 2004) is also plotted with a solid (dotted, dashed) line for  $\lambda = 1$  ( $\lambda = 0.1$ ,  $\lambda = 0.01$ ) with the bolometric correction same as that used in the previous section. For luminous AGNs with  $L_{2-10\text{keV}} > 10^{44} \text{ erg s}^{-1}$ , the limits of the stellar masses of the host galaxies are consistent with  $\lambda = 0.1$  or higher. For less luminous AGNs, the limits are still consistent with  $\lambda \sim 0.05$ . All of the upper limits of the stellar masses, except for GOODSS057 and GOODSS263, are consistent with  $\lambda = 1$ , which is different from Figure 7. The difference indicates that the mass to UV-light ratio of the accepted models with the largest mass are larger than those of the LBGs at  $z \sim 3$  for the ‘‘extended’’ AGNs.

#### 4.2.3. Stellar Mass Estimation of GOODSS027

A part of the GOODSS field is covered by the ACS and the NICMOS Ultra Deep Field (UDF). Using the deep optical and near-infrared data, we obtain better constraint of stellar masses for AGNs in the region. Four high- $z$  AGNs locate in the ACS UDF, and two of them, GOODSS027 and GOODSS091 are covered by the NICMOS UDF. GOODSS027 is mostly dominated by the host galaxy component. The radial profile of the galaxy is well fitted with the de Vaucouleurs profile without a nuclear stellar component in the ultra deep image. On the contrary, GOODSS091 image is dominated by a stellar component. By assuming that the contribution from a stellar nucleus is negligible for GOODSS027, we use the F110W and F160W magnitudes along with F606W, F775W, F850LP, and the ISAAC  $K_S$ -band magnitudes to obtain a better constraint on the stellar mass of the object.

In order to conduct SED fitting, we derived aperture magnitudes in the F606W, F775W, F850LP, F110W, and F160W bands by adjusting the PSF size in all of the 5 images to that in the F160W band (FWHM of  $0.''38$ ). We used a  $2.''6$  diameter to derive the SED of the object. In order to convert the aperture magnitudes to total magnitudes used in the  $K$ -band, we add the difference between the aperture and total magnitude in the F775W band to the aperture magnitudes. We fit the photometric data points with the stellar synthesis model spectra for E and Sb derived in the previous section. For the object, we use  $\chi^2$  minimization method to derive the best fit synthesis model. The best fit model is shown in Figure 11. It is the Sb model at 1800 Myr with  $E(B-V) = 0.5$  mag and a stellar mass of  $5.3 \times 10^{11} M_{\odot}$ . The model is similar to the largest mass model of the object in the previous subsection. The mass of the best fit model is shown with the star mark in Figure 10. The stellar mass of the model is close to the largest mass model of the object in the previous subsection. The result is reasonable, because the upper limit of the mass in the previous section is defined by the spectral model that follows the total magnitudes in the F660W, F775W, F850LP, and  $K_{AB}$  bands. The derived stellar mass is larger than the upper limits on the stellar masses of the other ‘‘extended’’ AGNs.

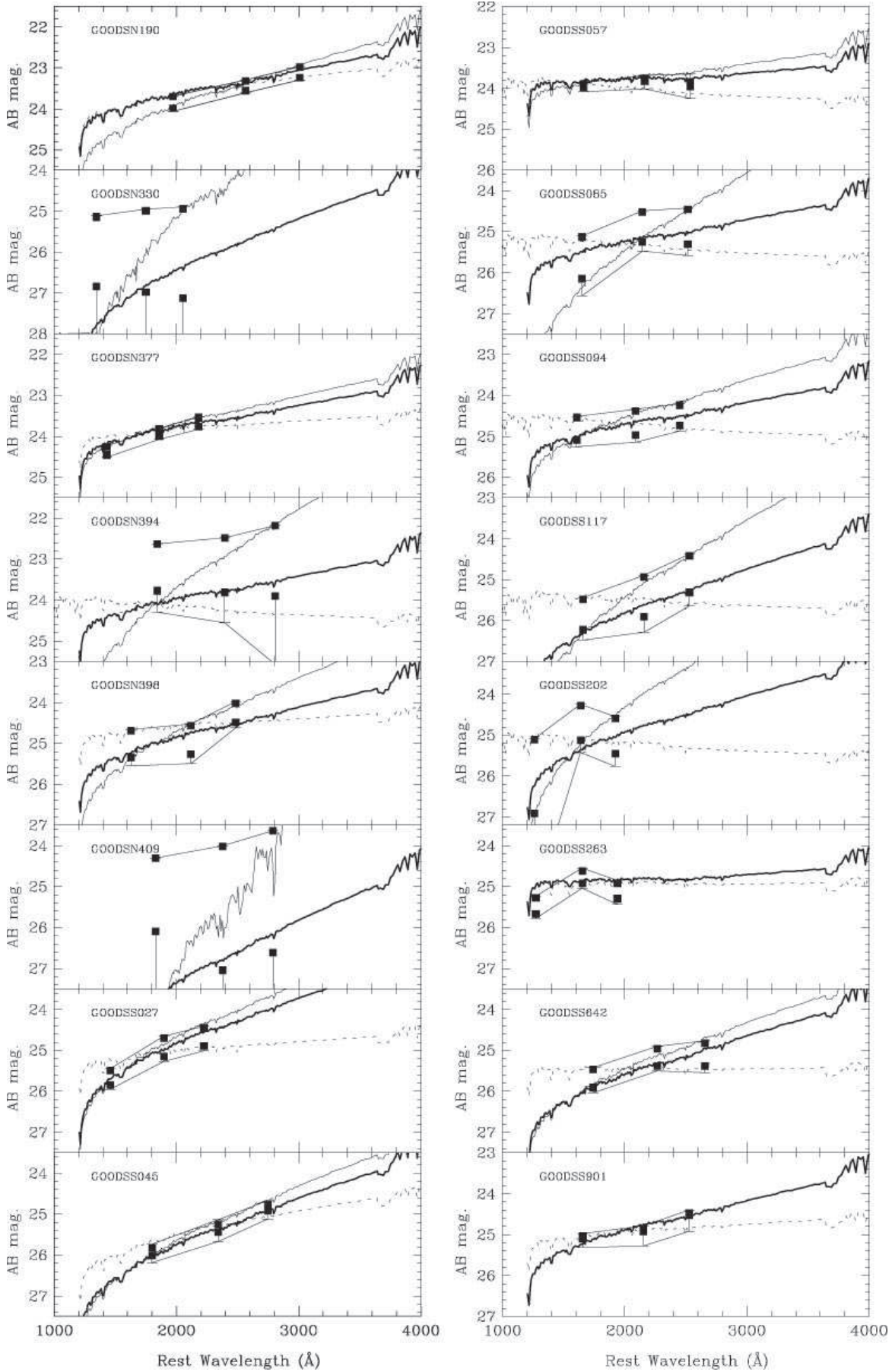


FIG. 8.— Upper and lower limits of the brightness of the host galaxies of the “extended” AGNs are shown with filled squares connected with solid lines, along with the SEDs of the accepted models with the largest (thin solid line) and smallest (thin dashed line) stellar mass. The horizontal axis is the object-frame wavelength and the vertical axis is the observed AB magnitude. The models which do not exceed the upper and the lower limits in the F606W, F775W, and F850LP bands simultaneously with a certain normalization are accepted. The thick solid line indicates the largest stellar mass model consistent with the observed  $K_{AB}$ -band magnitude.

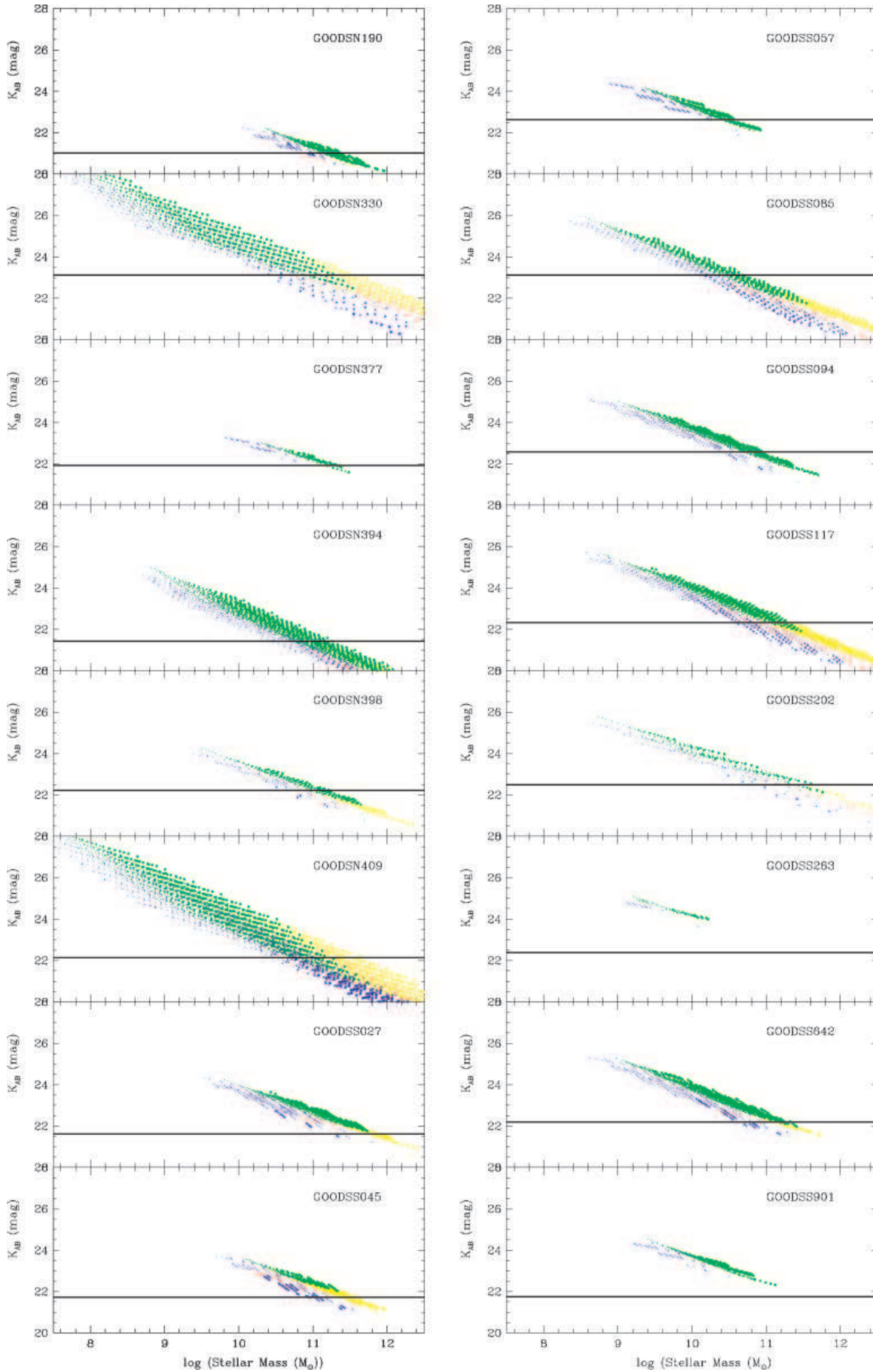


FIG. 9.— Distribution of  $K_{AB}$ -magnitudes and stellar masses of the accepted models of each AGN. Large, medium, and small marks corresponds to models with age larger than 1000Myr, between 1000Myr and 500Myr, and smaller than 500 Myr, respectively. The red (yellow) and blue (green) points mean E (Sb) models with  $E(B-V) > 0.5(\text{mag})$  and  $E(B-V) < 0.5(\text{mag})$ . The horizontal thick solid line indicates the observed  $K_{AB}$ -magnitude of the AGN.

TABLE 5  
LIMITS ON THE STELLAR MASSES OF THE HOST GALAXIES OF THE “EXTENDED” AGNS

Name	Accepted Model with the Largest Mass				Accepted Model with the Smallest Mass			
	Type	Age (Myr)	$E(B-V)$ (mag)	$\log(\text{Mass}) (M_{\odot})$	Type	Age (Myr)	$E(B-V)$ (mag)	$\log(\text{Mass}) (M_{\odot})$
GOODSN190	Sb	3000	0.3	11.36	E	160	0.3	10.06
GOODSN330	Sb	1000	0.7	11.50	E	120	0.0	7.40
GOODSN377	Sb	1600	0.3	11.31	E	120	0.2	9.82
GOODSN394	Sb	2500	0.3	11.20	E	120	0.0	8.72
GOODSN398	Sb	2000	0.4	11.21	E	120	0.2	9.38
GOODSN409	Sb	2500	0.8	11.63	E	120	0.0	7.28
GOODSS027	Sb	1600	0.6	11.93	E	180	0.2	9.54
GOODSS045	Sb	2500	0.6	11.57	E	140	0.4	9.70
GOODSS057	Sb	2000	0.1	10.56	E	120	0.0	8.89
GOODSS085	Sb	2000	0.3	10.69	E	120	0.0	8.36
GOODSS094	Sb	2000	0.3	10.93	E	120	0.0	8.64
GOODSS117	Sb	1200	0.6	11.27	E	200	0.0	8.58
GOODSS202	Sb	1400	0.5	11.60	E	120	0.0	8.67
GOODSS263	Sb	1400	0.1	10.22	E	120	0.1	9.12
GOODSS642	Sb	2500	0.5	11.32	E	120	0.1	8.61
GOODSS901	Sb	1800	0.4	11.12	E	120	0.2	9.23

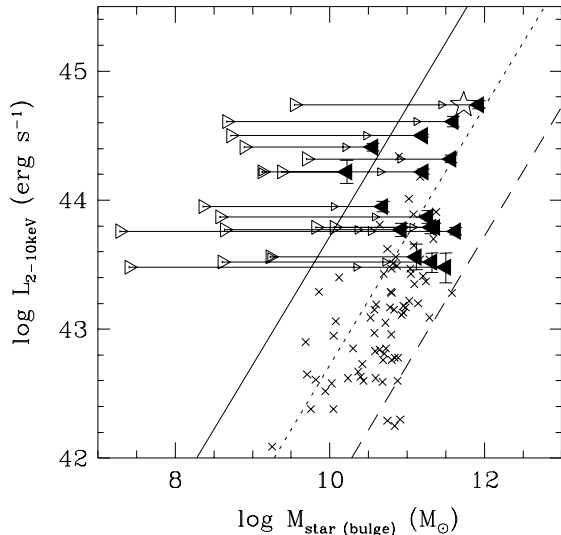


FIG. 10.— Distribution of stellar mass and  $L_{2-10\text{keV}}$  of the “extended” AGNs. Upper and lower limits are shown with filled and open triangles, respectively. The small rightward open triangles indicate the lower limits in case that the host galaxy component dominates the whole  $K_{AB}$ -band magnitude. Horizontal solid lines indicate the allowed range of the stellar mass. The star mark show the stellar mass of the best fit model for GOODSN027 shown in Figure 11. Crosses show the distribution of the bulge stellar masses of the X-ray selected low-redshift AGNs from Schade et al. (2000). The solid line indicates  $\lambda = 1$ , the bolometric correction of 25, and  $M_{\bullet}/M_{\text{bulge}} = 0.0014$ . The dotted and dashed lines indicate the cases with  $\lambda = 0.1$  and  $0.01$ , respectively.

### 5.1. Comparison with Properties of Galaxies at $2 < z < 4$

The object-frame UV absolute magnitudes of the host galaxies of the X-ray-selected AGNs at  $2 < z_{\text{sp}} < 4$  are distributed within a order of magnitude of the typical (knee of the luminosity function) UV absolute magnitude of the LBGs at  $z \sim 3$ . The inferred star formation rates are less than  $40 M_{\odot} \text{ yr}^{-1}$  for most of them, also which are similar to those of LBGs. The constraints on the star-formation rates of the host galaxies reject apparently large ( $> 100 M_{\odot} \text{ yr}^{-1}$ ) star formation rates

which are observed in high- $z$  ultra-luminous QSOs, if we neglect the effect of dust extinction. The observed SEDs of the “extended” AGNs allow the synthesis models with a young stellar population affected by  $E(B-V) = 0.5$  mag, which corresponds to  $A_{1700} = 4.8$  mag with the Calzetti extinction curve. This means the reddening correction of up to 2 orders of magnitude is still possible, and we cannot reject the large star formation rate in the high- $z$  host galaxies. It should be noted that we cannot constrain violent star formation within 1kpc of the nucleus, because such component cannot be distinguished from the nuclear stellar component due to the resolution of the observation.

The estimated upper limits of the stellar mass of the host galaxies of the “extended” AGNs ( $\sim 10^{10} M_{\odot} - 10^{11} M_{\odot}$ ) corresponds to the stellar mass of the  $z \sim 3$  LBGs with relatively large stellar mass ( $\sim 10^9 M_{\odot} - 10^{11} M_{\odot}$ ; Papovich et al. 2001; Shapley et al. 2001), and similar to those of red galaxies at  $z \sim 2$  ( $2 \times 10^{10} M_{\odot} - 5 \times 10^{11} M_{\odot}$  for Distant Red Galaxies, DRGs; Förster et al. 2004; van Dokkum et al. 2004). The estimated upper limits are one order of magnitude smaller than radio galaxies, which have the largest stellar mass at each redshift (Rocca-Volmerange et al. 2004). The lower limits of the stellar mass are consistent with those of the LBGs at  $z \sim 3$  with small stellar mass.

### 5.2. Comparison of the $M_{\text{bulge}} - M_{\bullet}$ relation with that of AGNs at Low-Redshifts

In order to compare the  $M_{\text{bulge}} - L_{2-10\text{keV}}$  distribution of the “extended” AGNs with that of AGNs in the nearby universe, we also plot the bulge stellar masses and  $L_{2-10\text{keV}}$  of Einstein Medium Sensitivity Survey (EMSS) sample of AGNs at  $z < 0.15$  from Schade et al. (2000) with crosses. Their bulge  $R_{AB}$ -band absolute magnitudes are estimated based on their bulge apparent  $I_{AB}$ -band magnitudes, which are determined from a snap-shot imaging survey with the HST and with a color of an Sb galaxy at  $z = 0$  ( $R_{AB} - I_{AB} = 0.65$  mag). To convert the  $R_{AB}$ -band absolute magnitude to a bulge stellar mass, we use the average mass-to-light ratio of bulge component of early-type galaxies (4.1 in  $R$ -band; Haring & Rix 2004). Their  $L_{2-10\text{keV}}$  are derived from 0.5–3.5 keV flux mea-

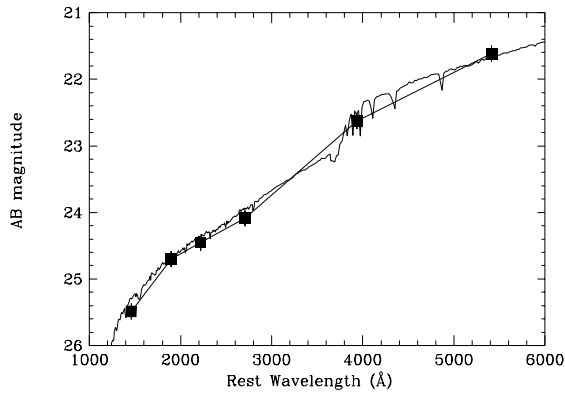


FIG. 11.— F606W to  $K_s$ -band SED of GOODSS27 shown with filled squares and error bars along with the best fit model SED. The horizontal axis is the object-frame wavelength and the vertical axis is the observed AB magnitude.

sured in the EMSS survey by assuming a photon index of 1.8. The nearby AGN sample distribute between  $\lambda = 0.01 - 1$ , and most of them are concentrate between  $\lambda = 0.01 - 0.1$ . The distribution is consistent with the similar plot with optical nuclear absolute magnitude and bulge absolute magnitude which suggests  $\lambda < 0.1$  for most of them (Schade et al. 2000; Dunlop et al. 2003; Jahnke, Kuhlbrodt, & Wisotzki 2004). With nuclear hard X-ray luminosity, Miyaji et al. (2004) also obtained a similar result at intermediate redshift. However, even in the low redshift universe, still the distribution is not well established (Sanchez et al. 2004).

The estimated stellar mass limits are similar to the the estimated stellar masses of the spheroidal components of nearby AGNs with lower luminosity as shown in Figure 10. If we assume the high- $z$  AGNs have the same  $\lambda$  as the nearby AGNs and follow the same  $L_{2-10\text{keV}}$  and  $M_\bullet$  relation, the stellar mass of the high- $z$  AGNs have to be smaller than that of a galaxy with the same black hole mass in the nearby universe. This implies that the black hole grew faster than the stellar component in the host galaxy. Considering the  $M_{\text{bulge}} - M_\bullet$  relation in the nearby universe, the high- $z$  host galaxies require to grow at least 3–10 times, accumulate more than  $10^{11} M_\odot$  in stellar mass, from  $z = 2 \sim 4$  to  $z = 0$  under the assumption that the black hole already reaches its final mass at  $z = 0$ . The look back time of redshift 2 (4) is 10.2 (12.0) Gyr, thus if star formation continues with the upper limits of the inferred star formation rates ( $< 40 M_\odot \text{ yr}^{-1}$ ) in the host galaxies, it is still possible to gain  $10^{11} M_\odot$  of stars. However, the black holes also can grow up since  $z = 2 - 4$ . An estimated average black hole growth history of black holes with final  $z = 3$  mass of about  $10^8 M_\odot$  indicates that the mass at  $z = 2 \sim 4$  is only 10 ~ 30% in comparison with the final  $z = 0$  mass (Marconi et al. 2003).

Alternatively, it is also possible that the high- $z$  AGNs have larger  $\lambda$  value than the nearby AGNs. The black hole mass estimations of the optically-selected luminous QSOs derived from the width of the optical broad emission line and the absolute magnitude suggest that the Eddington ratio reaches 1 for a significant fraction of luminous AGNs (Woo & Urry 2002; Vestergaard 2004; McLure & Dunlop 2003; Warner, Hamann, & Dietrich 2004). For example, 27% of the AGNs have  $\lambda$  larger than 1 in Warner et al. (2004). The fraction gets higher for AGNs with larger luminosity. For low-luminosity AGNs, the estimated Eddington ratios are mostly distributed between 0.01 and 0.1 (e.g., Schade et al. 2000), systematically smaller than those observed in luminous AGNs (McLure & Dunlop 2003).

In order to distinguish the two possibilities, it is necessary to determine the mass of the central black hole of high-redshift AGNs by an independent way. For non-obscured “compact” AGNs, using the CIV line width (3000–5000  $\text{ks s}^{-1}$  for GOODSS AGNs; Szokoly et al. 2003) and the total  $M_{1700\text{AB}}$ , we can estimate the central black hole mass (e.g. (4) in Warner, Hamann, & Dietrich 2003). The estimated masses of the black holes are  $1 \sim 4 \times 10^8 M_\odot$  for  $L_{2-10\text{keV}} = 10^{45} \text{ erg s}^{-1}$  and  $1 \sim 4 \times 10^7 M_\odot$  for  $L_{2-10\text{keV}} = 10^{44} \text{ erg s}^{-1}$  AGNs. It is assumed that the absolute magnitude is not affected by the extinction. These masses indicate  $\lambda = 0.3 - 1.3$ , which are larger than those of low-luminosity AGNs in the nearby universe and similar to high-luminosity AGNs. If the “extended” AGNs have the same  $\lambda$  for the “compact” AGNs, all of the mass limits of the host galaxies are consistent with the  $M_{\text{bulge}} - M_\bullet$  relation in the nearby universe.

The estimated stellar mass ranges of the high-redshift host galaxies do have uncertainty of one order of magnitude even for the “extended” AGNs. In order to reduce the uncertainty, better constraints on the host galaxy apparent  $K$ - (or  $H$ -) band magnitude is crucial, and additional  $J$ -band information is helpful. Ground-based AO system will provide us unique high-angular resolution images in the near-infrared bands (e.g., Croom et al. 2004). Currently observable sample is restricted, only to relatively bright QSOs selected from the huge sample of QSOs found in shallow wide area survey (like 2Qz, 2dF QSO survey), due to lack of natural guide star. The limitation will be very much eased with laser guide star system in the near future. Moreover, the improvements of AO system with higher frequency corrections enable us to obtain high-resolution images in the shorter wavelength range, such as  $J$ -band, constantly.

The author would like to thank Drs. Kouji Ohta, Kazuhiro Sekiguchi, Tadafumi Takata, Yoshihiro Ueda, and Kentaro Aoki for their detailed and invaluable comments. M.A. acknowledge support from a Research Fellowship of the Japan Society for the Promotion of Science for Young Scientists.

#### REFERENCES

- Abraham, R.G., Valdes, F., Yee, H.K.C., & S. van den Bergh 1994, *ApJ*, 432, 75  
 Alexander, D.M., et al. 2003, *AJ*, 126, 539  
 Barger, A.J., Cowie, L. L., Cowie, L.L., Trentham, N., Fulton, E. Hu, E.M., Songaila, A., & Hall, D. 1999, *ApJ*, 117, 102  
 Barger, A.J., Cowie, L. L., Bautz, M. W., Brandt, W. N., Garmire, G. P., Hornschemeier, A. E., Ivison, R. J., Owen, F. N. 2001, *AJ*, 122, 2177  
 Barger, A.J., Cowie, L.L., Capak, P., Alexander, D.M., Bauer, F.E., Fernandez, E., Brandt, W.N., Garmire, G.P., & Hornschemeier, A.E. 2003, *AJ*, 126, 632  
 Bertin, E., & Arnouts, S. 1996, *A&AS*, 117, 393  
 Bertoldi, F., Cox, P., Neri, R., Carilli, C.L., Walter, F., Omont, A., Beelen, A., Henkel, C., Fan, X., and Strauss, M.A., Menten, K.M. 2003, *A&A*, 409, L47  
 bou03] Bouwens, R., Broadhurst, T., & Illingworth, G. 2003, *ApJ*, 593, 640  
 Boyle, B.J., Terlevich, R. J. 1998, *MNRAS*, 293, 49  
 Calzetti, D., Armus, L., Bohlin, R.C., Kinney, A.L., Koornneef, J., Storchi-Bergmann, T. 2000, *ApJ*, 533, 682  
 Cohen, J.G., Hogg, D.W., Blandford, R., Cowie, L.L., Hu, E., Songaila, A., Shopbell, P., & Richberg, K. 2000, *ApJ*, 538, 29

- Corbett, E.A., Croom, S.M., Boyle, B.J., Netzer, H., Miller, L., Outram, P.J., Shanks, T., Smith, R.J., Rhook, K. 2003, *MNRAS*, 343, 705
- Cowie, L.L., Barger, A.J., Hu, E.M., Capak, P., & Songaila, A. 2004, *AJ*, 127, 3137
- Croom, S., Schade, D., Boyle, B.J., Shanks, T., Miller, L., Smith, R. 2004, *ApJ*, 606, 126
- Dawson, S., McCrady, N., Stern, D., Eckart, M.E., Spinrad, H., Liu, M.C., & Graham, J.R. 2003, *ApJ*, 125, 1236
- Dunlop, J.S., McLure, R.J., Kukula, M.J., Baum, S.A., O'Dea, C.P., & Hughes, D.H. 2003, *MNRAS*, 340, 1095
- Falomo, R., Kotilainen, J.K., Pagani, C., Scarpa, R., Treves, A. 2004, *ApJ*, 604, 495
- Fioc, M., & Rocca-Volmerange, B. 1997, *A&A*, 326, 950
- Förster, N.M., et al. 2004, *ApJ*, in press, astro-ph/0408077
- Franceschini, A., Hasinger, G., Miyaji, T., & Malquori, D. 1999, *MNRAS*, 310, 5
- Fruchter, A.S., & Hook, R.N. 2002, *PASP*, 114, 144
- Gebhardt, et al. 2000, *ApJ*, 539, L13
- Giacconi, R., et al. 2002, *ApJS*, 139, 369
- Giavalisco, M., et al. 2004, *ApJ*, 600, L93
- Hamann, R., & Ferland, G. 1999, *ARA&A*, 37, 487
- Haring, N., & Rix, H. 2004, *ApJ*, 604, L89
- Isaak, K.G., Priddy, R.S., McMahon, R.G., Omont, A., Peroux, C., Sharp, R., & Withington, S. 2002, *MNRAS*, 329, 149
- Jahnke, K., et al. 2004, astro-ph/0403462
- Jahnke, K., Kuhlbrodt, B., & Wisotzki, L. 2004, *MNRAS*, 352, 399
- Le Borgne, D. & Rocca-Volmerange, B. 2002, *A&A*, 386, 446
- Kodama, T., & Arimoto, N. 1997, *A&A*, 320, 41
- Kormendy, J., & Richstone, D. 1995, *ARA&A*, 33, 581
- Kukula, M.J., Dunlop, J.S., McLure, R.J., Miller, L., Percival, W.J., Baum, S.A., & O'Dea, C.P. 2001, *MNRAS*, 326, 1533
- Madau, P., Pozzetti, L., & Dickinson, M. 1998, *ApJ*, 498, 106
- Magorrian, J., et al. 1998, *AJ*, 115, 2285
- Marconi, A., & Hunt, L.K. 2003, *ApJ*, 589, L21
- Marconi, A., Risaliti, G., Gilli, R., Hunt, L.K., Maiolino, R., Salvati, M. 2004, *MNRAS*, 351, 169
- McLure, R.J., & Dunlop, J.S. 2004, *MNRAS*, 352, 1390
- Merritt, D., Ferrarese, L. 2001, *MNRAS*, 320, 30
- Miyaji, T., Sarajedini, V., Griffiths, R.E., Yamada, T., Schurch, M., Cristbal-Hornillos, D., & Motohara, K. 2004, *AJ*, 127, 3180
- Netzer, H. 2003, *ApJ*, 583, L5
- Omont, A., Beelen, A., Bertoldi, F., Cox, P., Carilli, C.L., Priddey, R.S., McMahon, R.G., Isaak, K.G. 2002, *A&A*, 398, 857
- Papovich, C., Dickinson, M., & Ferguson, H.C. 2001, *ApJ*, 559, 620
- Ridgway, S.E., Heckman, T.M., Calzetti, D., & Lehnert, M. 2001, *ApJ*, 550, 122
- Rocca-Volmerange, B., Le Borgne, D., De Breuck, C., Fioc, M., & Moy, E. 2004, *A&A*, 415, 931
- Sanchez, S.F., et al. 2004, *ApJ*, submitted, astro-ph/0403645
- Shapley, A.E., Steidel, C.C., Adelberger, K.L., Dickinson, M., Giavalisco, M., & Pettini, M. 2001, *ApJ*, 562, 95
- Schade, D.J., Boyle, B.J., Letawsky, M. 2000, *MNRAS*, 315, 498
- Shields, G.A., Gebhardt, K., Salviander, S., Wills, B.J., Xie, B., Brotherton, M.S., Yuan, J., & Dietrich, M. 2003, *ApJ*, 583, 124
- Steidel, C.C., Adelberger, K.L., Giavalisco, M., Dickinson, M.E., & Pettini, M. 1999, *ApJ*, 519, 1
- Szokoly, G.P., et al. 2003, *ApJS*, in press, astro-ph/0312324
- Ueda, Y., Akiyama, M., Ohta, K., & Miyaji, T. 2003, *ApJ*, 598, 886
- Yamada, T. 1994, *ApJ*, 423, L27
- Yu, Q., & Tremaine, S. 2002, *MNRAS*, 335, 965
- van Dokkum, P.G., et al. 2004, *ApJ*, 611, 703
- Vestergaard, M. 2004, *ApJ*, 601, 676
- Warner, C., Hamann, F., & Dietrich, M. 2003, *ApJ*, 596, 72
- Warner, C., Hamann, F., & Dietrich, M. 2004, *ApJ*, 608, 136
- Woo, J., & Urry, C.M. 2002, *ApJ*, 579, 530